

Perceiving, Predicting, and Planning: Robotic Expeditionary Science in Spatiotemporal Fields

by

Victoria Lynn Preston

B.S. 2016, OLIN COLLEGE OF ENGINEERING

S.M. 2019, MASSACHUSETTS INSTITUTE OF TECHNOLOGY

Submitted to the Department of Aeronautics and Astronautics and the Joint Program in Oceanography and Applied Ocean Science & Engineering in partial fulfillment of the requirements for the degree of Doctor of Philosophy in Autonomous Systems

at the

MASSACHUSETTS INSTITUTE OF TECHNOLOGY

and the

WOODS HOLE OCEANOGRAPHIC INSTITUTION

©2022 V. Preston. All rights reserved.

The author hereby grants to MIT and WHOI permission to reproduce and to distribute publicly copies of this thesis document in whole or in part in any medium now known or hereafter created.

Author
Department of Aeronautics and Astronautics, MIT
Applied Ocean Science & Engineering, WHOI
December 12th, 2022

Certified by
Nicholas Roy
Bisplinghoff Professor of Aeronautics and Astronautics, MIT
Thesis Supervisor

Certified by
Anna Michel
Associate Scientist with Tenure, Applied Ocean Physics and Engineering, WHOI
Thesis Supervisor

Accepted by
Jonathan P. How
R. C. Maclaurin Professor of Aeronautics and Astronautics, MIT
Chair, Graduate Program Committee

Accepted by
David Ralston
Associate Scientist with Tenure, Applied Ocean Physics & Engineering, WHOI
Chair, Joint Committee for Applied Ocean Science & Engineering

Perceiving, Predicting, and Planning: Robotic Expeditionary Science in Spatiotemporal Fields

by

Victoria Lynn Preston

Submitted to the Department of Aeronautics and Astronautics and the Joint Program in Applied Ocean Science & Engineering on December 12th, 2022 in partial fulfillment of the requirements for the degree of Doctor of Philosophy

ABSTRACT

Making measurements of the natural world and building accurate models is crucial to understanding our environment and the spatiotemporal processes that drive our climate. Autonomous robots are especially well-suited to gathering those measurements efficiently. However, to collect useful observations of unknown, partially-observed spatiotemporal distributions for scientific inquiry requires accurately perceiving a phenomenon of interest, predicting how it will evolve in time, and planning effective sampling trajectories, potentially under severe operational constraints.

Thesis Supervisor: Nicholas Roy

Title: Bisplinghoff Professor of Aeronautics and Astronautics, MIT

Thesis Supervisor: Anna Michel

Title: Associate Scientist with Tenure, Applied Ocean Physics and Engineering, WHOI

CONTENTS

1	INTRODUCTION	16
2	PROBLEM SETTING	17
2.1	Science Background	18
2.2	Robotics Background	18
3	BACKGROUND AND RELATED WORK	19
4	OPERATIONS AT SEA	20
4.1	Challenges in the Deep Ocean	20
4.2	Overview of Science Teams and Responsibilities	20
4.3	Data Infrastructure on a Vessel	20
4.4	Taking Ground Truth Measurements	20
4.4.1	Water Column Standards	20
4.4.2	Hydrothermal Vents	20
4.4.3	Crossflow	21
5	DISCOVERING HYDROTHERMALISM FROM AFAR	22
5.1	Introduction	22
5.2	Materials and Methods	24
5.2.1	Site Description	24
5.2.2	Sampling Platforms and Instruments	26
5.2.3	Analytical Procedure	29
5.2.4	Transect Design and Execution	30
5.3	Results	31
5.3.1	Methane Observations from Spectroscopic Instruments	31
5.3.2	Methane and Ammonium Observations with the Rosette	32
5.3.3	Turbidity	33
5.3.4	Oxidation Reduction Potential	34
5.3.5	Temperature, Salinity, and Oxygen	35

5.4	Discussion	37
5.4.1	Sensor Cross-Correlations	37
5.4.2	Hydrothermalism Detection via Time-Series Regimes	40
5.4.3	Methane in Deep Sea Exploration	42
5.4.4	Enabling Better Decision-Making for Hydrothermalism Discovery	43
6	PHYSICALLY-INFORMED OPERATIONAL ROBOTIC TRAJECTORIES FOR SCIENTIFIC EXPEDITIONS	45
6.1	Introduction	45
6.1.1	Charting Deep-Sea Hydrothermalism	48
6.1.2	Closing the Loop: Expedition Logistics for Deep-Sea Robotics .	51
6.1.3	Contributions	52
6.2	Problem Formulation	54
6.2.1	Scientific Expeditions as a Sequential Decision-Making Problem	54
6.2.2	Sequential Decision-Making with AUV <i>Sentry</i>	55
6.2.3	Charting Hydrothermalism as a POMDP	56
6.3	Methodology	59
6.3.1	Plume Detection: Treatment of Robotic Science Sensors	59
6.3.2	External Sensing: Leveraging All Available Information	62
6.3.3	PHUMES: Physically-informed Probabilistic Forecasts	63
6.3.4	Trajectory Optimization for Path Planning with Fixed Primitives	67
6.3.5	At Sea Operations	68
6.4	Field Deployment: Charting Deep-Sea Hydrothermal Plumes	68
6.4.1	Site Description and General Conditions	69
6.4.2	Overview of Sea Trials with AUV <i>Sentry</i>	71
6.4.3	Experimental Results	72
7	PLANNING: ADAPTIVE SAMPLING IN SPATIOTEMPORAL FIELDS	75
7.1	Underway Autonomy: PLUMES	75
7.2	Deployment-by-Deployment Autonomy: PHORTEX	75
7.3	Field Results in GB	75
7.4	Summary	75
8	DISCUSSION	76
8.1	Generalizing to Other Domains	76
8.2	Open Challenges	76

8.3	Embedding Autonomy Engineers into Science Teams	76
8.4	Robotics in Expeditionary Science	76
9	LOOKING FORWARD	77
A	PERCEIVING	78
A.1	Method for Methane Measurement from Niskin Bottles	78
A.2	Leg 2 Niskin Bottle Sample Schedule and Measurements	80
A.3	Normalized Pythia Calibration	80
A.4	Depth-Correction	82
A.5	Description of Plume Model for Transect Design	82
	ACRONYMS	86
	GLOSSARY	87

LIST OF FIGURES

5.1	Overview of general transect design. Plumes generated by black smoking chimneys at an active hydrothermal ridge in the Northern Guaymas Basin (one example pictured here, taken with an arm mounted MISO camera by ROV <i>JASON</i> during RR2107) rise approximately 175 m in the water column and are advected and turbulently mixed with background seawater. AUV <i>Sentry</i> and a towed CTD rosette, both equipped with turbidity, oxygen, temperature, salinity, and methane probes, fly trajectories that aim to intersect the lower and upper neutrally buoyant plume layer, respectively. A comparison of the observations collected by both platforms is then used to demonstrate the efficacy of various sensors and algorithmic detection schemes.	25
5.2	AUV <i>Sentry</i> and a towed rosette were used to perform coincident several kilometer long trajectories in the Northern Guaymas Basin. The rosette was redeployed mid-trajectory in order to empty the Niskin bottles onboard; this split the rosette trajectory into Leg 1 and Leg 2. The trajectories intersected a region of known hydrothermal activity in the northern basin; a bathymetric relief of this region is overlaid on the far right panel. The red star on the bathymetric relief marks the nearest point of identified hydrothermal activity (black smokers) relative to the trajectories (27.407489 N, 111.389893 W), and is used as a reference point in this work. Imagery is provided by the GoogleTiles API in Cartopy. The bathymetric relief is rendered using data collected by AUV <i>Sentry</i> during research cruise RR2107.	26
5.3	The SAGE and Pythia instruments mounted on the rosette and AUV <i>Sentry</i> , respectively.	28

5.4 Normalized methane values observed with both SAGE (rosette) and Pythia (<i>Sentry</i>) over reference distance from (27.407489 N, 111.389893 W). The transect begins at the left of the plot and proceeds to the right. Strong methane anomalies, defined as points above a conservative threshold of 0.5 normalized values, are present starting 3 km from the reference source as observed by Pythia, and 1.5 km as observed by SAGE (open green circles).	32
5.5 Normalized methane measurements by SAGE plotted with methane measurements taken from Niskin bottle samples (as measured by DGEU/GGA equipment) and ammonium measurements. Bottle methane measurements are reported as a range to reflect sensitivity of the measurement procedure to a calibrated extraction efficiency. All measurements trend towards a peak observation of methane and ammonium 0.75 km from the reference source. SAGE additionally observes a secondary peak approximately 2 km from the source, which is essentially missed by the bottle sample schedule.	33
5.6 Turbidity observed as beam attenuation on the rosette transmissometer and optical backscatter on AUV <i>Sentry</i> instruments. <i>Sentry</i> encountered a sensor error until approximately 4.5 km from the ridge reference point. After this point, elevated turbidity is detectable throughout the dive, with significant elevations within 3.3 km east of the ridge reference point, dissipating within tens of meters to the west. Elevated turbidity is observed by the rosette 2.2 km from the ridge reference point to the east.	34
5.7 The derivative of ORP observed by data collected on AUV <i>Sentry</i> . Negative slopes are indicative of entering hydrothermal fluids. Only one region of the transect demonstrated a significant reaction to ORP, within 200 m of the reference point.	35

5.8	Depth-corrected oxygen, temperature, and salinity over reference distance. Two notable regions of high temperature deviation from expected temperature are observed between 6-12 km (rosette; 8-11 km by <i>Sentry</i>) and within 3 km of the reference source. The first region of temperature anomaly is closely matched with fresher salinity measurements; whereas salinity is measured as marginally higher near the reference source by the rosette CTD and nominal or lower by the <i>Sentry</i> CTD. In both regions, oxygen is nominal or slightly depleted, with regions of notably elevated oxygen at the boundary of these regions.	36
5.9	Global Pearson correlation coefficient between sensors mounted on the rosette and <i>Sentry</i> . Correlation differences between Leg 1 (far from the reference point) and Leg 2 (near the reference point) are indicative of different sensor correlation behaviors with respect to ambient seawater conditions and hydrothermal fluid interception. <i>Sentry</i> correlation coefficients reflect an expected relationship between temperature and methane (positive), methane and oxygen (negative), and turbidity and methane (positive) that may be stereotypically associated with hydrothermal fluids. In contrast, the Leg 2 rosette correlation factors do not meet this expectation, despite showing strong overall correlative structure. . . .	38
5.10	Local (rolling) Pearson correlation coefficients between sensors mounted on the rosette over 30 minute windows.	39
5.11	Local (rolling) Pearson correlation coefficient between sensors mounted on AUV <i>Sentry</i> over 30 minute windows.	40
5.12	Regimes, indicated as alternating blue and red regions, detected during the rosette transect with a 30 minute detection window.	41
5.13	Regimes, indicated as alternating blue and red regions, detected during the AUV <i>Sentry</i> transect with a 30 minute detection window.	42

6.1 An overview of PHORTEX: **P**Hysically-informed **O**perational **R**obotic **T**rajectories for **E**Xpeditions. Over the course of an expedition, an autonomous vehicle is deployed several times. In preparation for a deployment, PHUMES is used to generate a probabilistic forecast of the target spatiotemporal distribution. PHUMES can be seeded with prior information from scientific knowledge, data of opportunity from other deployed sensing equipment, or previous robot deployments. A trajectory optimizer is given the forecasts and modifies the parameters of a trajectory primitive. Several primitives are chained together to form a complete deployment trajectory. The robot is then deployed and executes the trajectory. Following a deployment, *in situ* observations from multiple heterogeneous science sensors are collected from the robot and fused into a data product that can be used to train PHUMES, and the deployment planning process iterates. Here, the task of hydrothermal plume charting with AUV *Sentry* is illustrated. PHUMES generates an forecast of temporally-evolving plume centerlines and cross-sections from estimates of vent characteristics and fluid crossflow (e.g., current) informed by measurements or prior distributions over these variables. For a given height that *Sentry* can operate (and is constrained to operate for any given primitive), chains of uniform coverage lawnmowers are optimized (over parameters such as length, width, resolution, origin, and global angle) with respect to the plume forecast to intersect and track the plume over the course of a deployment window. Following a *Sentry* deployment, observation locations are classified as binary plume detections from analysis of several science sensors. This product is then used to update the PHUMES model of plume centerline and cross-section over time. The new PHUMES model is then used to plan the next deployment of *Sentry*. . .

48

- 6.2 Example time series (left) and associated detections (right) over the AUV *Sentry* sensor suite. Oxygen, temperature, and salinity measurements are detrended using a linear transformation fit to depth vs. value plots. The time series demonstrates two types of plume detections. The first are “obvious detections” in which most sensors register strong anomalies (this happened twice toward the end of the deployment) and are most strongly associated with buoyant-stem derived fluids. The second are “persistent-plume detections” in which the robot traverses through water that is slightly more turbid, warm, or chemical-rich than background water over potentially long horizons (this happened early in the deployment and in the middle). Such detections are most strongly associated with neutrally-buoyant layers. The conservative corroboration detector successfully identifies both forms of plume water. 61
- 6.3 PHUMES: PHysically-informed Uncertainty Models for Environment Spatiotemporality; a model class for forecasting spatiotemporal distribution evolution trained on partial observations. PHUMES generates forecasts by leveraging an embedded analytical model $f(\cdot, \cdot)$ that approximates the physics-driven evolution of a target distribution. This model is seeded with many samples from distributions placed over initial conditions, physical parameters, or temporal functions (such as \mathbf{x}_p and \mathbf{x}_c here). The composite result of this process is a forecast \mathbf{W} that consists of a mean and variance of phenomenon occupancy in a 3D volume over snapshots of time. This forecast is provided to a trajectory optimizer which sets a deployment trajectory that is executed by a robot. The deployment generates a series of observations, which are then used to update the distributions of the generating distributions via an MCMC procedure which compares the gathered observations with the simulated observations of samples from the generating distributions. The resulting posterior update over the generating distributions is then used for the next planning iteration. 65

6.4	The at-sea operations implementation of PHORTEX. Integration of scientific knowledge, prior information, auxiliary sensor information, and operational constraints was done at the initialization of the PHORTEX deployment-by-deployment loop. Every trajectory generated by PHORTEX was checked by AUV <i>Sentry</i> engineers and the science team before execution. <i>Sentry</i> status was monitored with an external acoustic tracking system that monitored vehicle location, power, and performance while in acoustic range of the ship. Upon returning to deck, all science sensor observations were downloaded in bulk from the vehicle, and then ingested via our PHORTEX system.	69
6.5	Study site in the Guaymas Basin, Gulf of California. The inset map is bathymetric data collected by AUV <i>Sentry</i> during this expedition and shows the approximately 600 m long ridge in yellow. The red star marks the chimney that was of particular study in this article. Pictures A-D show imagery from the ridge and chimney site. A-C show various forms of plume-producing vents located at the chimney and D shows an example of the macrofauna covering the structures along the ridge.	70
6.6	The four field dives of AUV <i>Sentry</i> . All data is plotted according to its detection identity (in-plume or seawater). The first column shows a top-view of the dive trajectories in polar coordinates, in which angle and radius is computed relative to the chimney coordinate of the vent of study. In the center column, the 3D path of the vehicle over the rendered bathymetric terrain is provided. All but Dive P-Plume were dives conducted in altitude-hold mode with <i>Sentry</i> , and so the trajectories show obvious changes in elevation; in contrast Dive P-Plume was held in depth-hold mode, so most observations are gathered within a depth-plane. The final column shows a time series versus depth of the detections collected. In Dive HP-Plume the portions of the dive that were human-designed and PHORTEX-designed are labeled with H and P, respectively. As can be seen in the Dive HP-Plume time series, the two human-designed trajectories have significantly different performance, despite being in locally similar regions of the spatial domain.	74
A.1	Fitted calibration curve for measurements of methane observed by Pythia.	81

A.2 Calibration curve, smoothing, and time correction applied to Pythia observations during the transect, before reported normalization in the manuscript.	82
A.3 Linear functions are fit to data collected for oxygen, temperature, and salinity instruments on each platform separately. A residual value is then computed for each observation.	83
A.4 A prototypical plume estimate according to the modified buoyant plume model in crossflow. The same envelope is plotted with respect to absolute depth (with a source located at 1850 m) on the left, and illustratively in the context of the hydrothermal ridge on the right.	85

LIST OF TABLES

6.1 Instruments on AUV <i>Sentry</i> and the criteria used to identify plume fluids for each instrument. The weight is used to indicate relative “trustworthiness” of a plume detection for each sensor, and is used in a corroboration scheme that sums detections across sensors in order to make a final determination on whether an observation location contained a parcel of plume fluid or consisted of background seawater. “Detrending” data removes depth-related cross-sensitivity from the measurements; for example, temperature is stratified in the deep ocean, so to ignore the impacts of depth changes in the data stream, those effects are removed by “detrending” the data stream.	60
6.2 Per-deployment statistics for field trials of PHORTEX. The deployment HP-Plume is broken further into human designed (H) and PHORTEX designed (P) portions for direct comparison.	73
A.1 Results of DGEU extraction efficiency calibration experiments.	79
A.2 Schedule of bottle samples during Leg 2 of rosette trajectory.	80
A.3 Geochemical measurements associated with the schedule of bottle samples during Leg 2 of rosette trajectory. Note that methane expressed in nM is computed using coincident temperature and salinity measurements during the transect as measured by rosette CTD, and extraction inefficiency of the DGEU is compensated for as described in Sec. A.1. . .	81
A.4 Parameter, vent characteristics, and ambient crossflow setting used for transect design.	85

1 INTRODUCTION

The environmental sciences are a multidisciplinary endeavor to understand the Earth, its ecosystems, and its processes, for which *in situ* observational studies or *expeditions* serve as the foundation on which scientific discovery and model development is predicated. Robots are uniquely well-positioned to advance long-term monitoring of and exploration in meso-scale planetary environments through autonomous expeditions. By virtue of their form, robots can be used in extreme places (e.g., deep sea), dangerous scenarios (e.g., edge of calving ice sheets), or long-term missions (e.g., Mars exploration). Increasingly, robotic platforms are being developed for scientific expeditions, but their autonomous capabilities are typically limited to predetermined hand-designed trajectories (e.g., uniform coverage lawnmowers [1]). This significantly restricts the class of phenomena that can be effectively studied by expeditionary scientific robots. For instance, spatiotemporal distributions—deep sea hydrothermal plumes, algal blooms, weather cells—can be severely under-sampled or missed using these strategies [2]. Given the ubiquity of these spatiotemporal phenomena and the cost of scientific field operations, it is critical to improve the efficacy of robots as autonomous scientific tools.

This thesis represents...

2 PROBLEM SETTING

To collect useful samples of a spatiotemporal field using a robotic platform is to pose a *sequential decision-making* problem. In this setting, we assume that the measurements that can be collected are partial observations of the unknown spatiotemporal environment, and the actions the robot can take in sequence are operationally constrained. We can formally state this problem as a partially observable Markov decision process (POMDP). Let $\Pi(\cdot)$ denote the space of probability distributions over the argument. A finite horizon POMDP can be represented as tuple: $(\mathcal{S}, \mathcal{A}, T, R, \mathcal{Z}, O, b_0, H, \gamma)$, where \mathcal{S} are the states, \mathcal{A} are the actions, and \mathcal{Z} are the observations. At planning iteration t , the agent selects an action $a \in \mathcal{A}$ and the transition function $T : \mathcal{S} \times \mathcal{A} \rightarrow \Pi(\mathcal{S})$ defines the probability of transitioning between states in the world, given the current state s and control action a . The transition function governs both how the state of the robot will evolve, given a chosen action, and the potentially stochastic evolution of the underlying spatiotemporal environment. After the state transition, the agent receives an observation according to the observation function $O : \mathcal{S} \times \mathcal{A} \rightarrow \Pi(\mathcal{Z})$, which defines the probability of receiving an observation, given the current state s and previous control action a . The reward function $R : \mathcal{S} \times \mathcal{A} \rightarrow \mathbb{R}$ serves as a specification of the task, assigning the states of the world that are useful for a given scientific objective high reward and others low reward. A POMDP is initialized with belief $b_0 \in \Pi(\mathcal{S})$ — an initial probability distribution over state — and plans over horizon $H \in \mathbb{Z}^+$ with discount factor $\gamma \in [0, 1]$.

As the robot moves through the world, it selects actions and receives observations. Since the state of the world is not directly observable in a POMDP, the robot maintains a probability distribution over possible states (i.e., belief) and must update this distribution each time it takes an action and receives an observation. Given the transition

and observation models, the belief can be updated directly using Bayes rule using a Bayes filter [3]:

$$\tau(b_{t-1}, a_{t-1}, z_t) = b_t \triangleq \Pi(S_t | a_0, z_0, \dots, a_{t-1}, z_{t-1}, z_t) \quad (2.1)$$

$$= \Pi(S_t | b_{t-1}, a_{t-1}, z_t) \quad (2.2)$$

$$= \frac{\int_{s \in \mathcal{S}} O(s, a_{t-1}, z_t) T(s, a_{t-1}, s') b_{t-1}(s')}{\Pi(z_t | b_{t-1}, a_{t-1})} \quad (2.3)$$

where $\tau(b, a, z)$ is the updated belief after taking control action a and receiving observation z (Eq. (6.3)). Unfortunately, Eq. (6.3) is intractable to compute directly and an approximate Bayesian inference procedure is required to represent the belief (e.g., Kalman filter [4], particle filter [5], or variational methods).

Due to the stochastic, partially observable nature of current and future states, the realized reward in a POMDP is a random variable. Optimal planning is defined as finding a horizon-dependent policy $\{\pi_t^* : \Pi(\mathcal{S}) \rightarrow \mathcal{A}\}_{t=0}^{H-1}$ that maximizes expected reward: $\mathbb{E}\left[\sum_{t=0}^{H-1} \gamma^t R(S_t, \pi_t(b_t)) | b_0\right]$, where b_t is the updated belief at time t , conditioned on the history of actions and observations. The recursively defined horizon- h optimal value function V_h^* quantifies, for any belief b , the expected cumulative reward of following an optimal policy over the remaining planning iterations: $V_0^*(b) = \max_{a \in \mathcal{A}} \mathbb{E}_{s \sim b}[R(s, a)]$ and

$$V_h^*(b) = \max_{a \in \mathcal{A}} \mathbb{E}_{s \sim b}[R(s, a)] + \gamma \int_{z \in \mathcal{Z}} \Pi(z | b, a) V_{h-1}^*(\tau(b, a, z)) dz \quad h \in [1, H - 1], \quad (2.4)$$

The optimal policy at horizon h is to act greedily according to a one-step look ahead of the horizon- h value function. However, Eq. (6.4) is intractable for large or continuous state, action, or observation spaces and thus the optimal policy must be approximated. Much of the art of practical decision-making uncertainty is making well-designed algorithmic and heuristic choices that enable efficient and robust planning algorithms.

2.1 SCIENCE BACKGROUND

2.2 ROBOTICS BACKGROUND

3 BACKGROUND AND RELATED WORK

- Defining Expeditionary Science
- Deep Ocean Research Definition
 - Hydrothermalism in the Deep Ocean
 - State of the Art Robots for Deep Ocean Research
- Planning Under Uncertainty
 - Informative Path Planning
- Representations for Spatiotemporal Distributions
 - Probabilistic: GPs, Bayesian Filters
 - Learned: NNs
 - Scientific Machine Learning: num GPs, PINNS
 - Numerical: models, NS, ODEs

4 OPERATIONS AT SEA

Preface that the intent of this chapter is to highlight practical engineering necessities and opportunities for deep sea research.

4.1 CHALLENGES IN THE DEEP OCEAN

No GPS, no satellite, only acoustics, very few observatories, etc.

4.2 OVERVIEW OF SCIENCE TEAMS AND RESPONSIBILITIES

Establish how computer scientists fit on a ship.

4.3 DATA INFRASTRUCTURE ON A VESSEL

Propose live-streaming...

4.4 TAKING GROUND TRUTH MEASUREMENTS

Basically impossible, some things more than others.

4.4.1 WATER COLUMN STANDARDS

Profiles gathered

4.4.2 HYDROTHERMAL VENTS

GEOCHEMICAL MEASUREMENTS

Jason wand/standard equipment

PHYSICAL MEASUREMENTS

Fluid exit velocity, PIV system

4.4.3 CROSSFLOW

Tiltmeters

5 DISCOVERING HYDROTHERMALISM FROM AFAR

[TODO: need a nicer intro paragraph to this section] To track a spatiotemporal phenomenon first requires sensing it. Expeditionary robots, in addition *ex situ* analysis containers for species collection, are typically equipped with a suite of heterogenous *in situ* sensors with varying field of views, accuracies, and noise models. In geochemical contexts in marine environments, these *in situ* sensors tend to yield continuous point observations for a proxy field (e.g., temperature, pressure, oxygen concentration), rather than precise measurements of an aggregate phenomenon (e.g., the presence of plume). The development of suitable *in situ* geochemical sensors for studying spatiotemporal phenomena with mobile sensor platforms is ongoing. For deep-sea research, the vast majority of carbonate cycle sensors (e.g., carbon dioxide, methane) developed for *in situ* use are severely limited by long response times (on the order of hours) and mismatched operating range. In this chapter, we examine the use to two novel *in situ* methane sensors for use in hydrothermal plume detection, and compare these geochemical sensors with other standard oceanographic equipment. We further detail methods for comparing sensor responses across heterogenous equipment to identify the presence of plume-derived fluids in the deep ocean. The content of this chapter was published in [6].

5.1 INTRODUCTION

Detecting and characterizing seafloor hydrothermal vents is critical in understanding the fundamental interactions among the geochemical and biological processes on the seafloor, and the fluxes that these processes cause to and from the deep ocean. Since the first discovery of deep sea hydrothermalism in 1977 [7], hundreds of hydrothermal venting sites have been discovered and analyzed [8]. These studies reveal that hydrothermal vents play a major role in ocean-scale elemental and micronutrient budgets

(e.g., [9, 10]), serve as nutrient pumps to the deep ocean (e.g., [11–14]), and sustain abundant and unique (e.g., chemosynthetic) forms of complex life [15, 16]. Hundreds of vent sites are hypothesized to exist and yet remain undiscovered in the deep ocean [8], limiting efforts to constrain nutrient and energy budgets of the deep ocean, to assess the magmatic budget hypothesis which estimates the global stock of hydrothermal activity, and to understand these novel ecosystems.

Exhaustive search of the seafloor is an impractical method for discovering new vents due to the scale of the ocean environment. Instead, adaptive surveying strategies and novel sensing technologies can be combined to detect hydrothermalism far (over 1 km laterally) from the plume source using water column observations. Hydrothermal plumes form due to a density difference between background seawater and (often significantly) heated vent fluids. The resulting buoyant force creates a coherent rising stem from the vent (the buoyant stem) and a spreading cloud (the neutrally-buoyant layer) at an isopycnal, when the cooling, mixing, hydrothermally-derived fluids reach equivalent density to the ambient background [17, 18]. The chemical composition of hydrothermal fluids differs greatly from that of background seawater and the plume-derived fluids near an active vent can be detected using most standard properties (i.e., temperature, salinity, chemical composition, turbidity). However, the spatial expression of the buoyant plume stem is typically no more than a few tens of square meters, making the buoyant stem difficult to localize on a survey. As emitted fluids travel further within the plume, the physically and chemically distinctive nature of the hydrothermal water mass is rapidly diluted as the plume entrains background seawater. Throughout this advective evolution of the plume, reactive (non-conservative) tracers can be consumed or transformed. Thus, despite the neutrally buoyant layer having a spatial scale extending for several square kilometers, detecting these plume fluids requires innovation in sensing and data analysis.

In this paper, we discuss the potential for water column-based hydrothermal plume discovery using standard sensing equipment (e.g., CTD, optode, transmissometer) in concert with two novel *in situ* methane instruments installed onboard an autonomous underwater vehicle (AUV) and a towed rosette. We present results from a field deployment at the northern Guaymas Basin in November 2021 and use these results to inform the planning of informative plume transects and the monitoring of real-time instrument responses. Both towed rosettes and AUVs are well-established tools for hydrothermal plume surveys. Rosettes deployed for hydrothermal plume hunting are typically used in either a vertical transect mode, or cast, performed at regularly spaced spatial way-

points along a ship transect, or a “towed” mode, in which the CTD is lowered and pulled through the water by the ship’s motion (e.g., [19, 20]). AUVs, by virtue of being untethered from the ship, have the ability to finely control location within the water volume, and can typically operate closer to the seafloor than a towed rosette. Standard sensors mounted on either a rosette or AUV can detect different forms of hydrothermalism. High turbidity several hundred meters from the seafloor may be indicative of a neutrally-buoyant plume generated by a black smoker, whereas changes in oxidation-reduction potential and clear waters near the seafloor may be indicative of diffuse flow. Analyzing these sensors individually and in combination can disambiguate these types of hydrothermalism and elucidate plume structure and characteristics of venting sources on the seafloor.

In 2021, our expedition aboard the R/V *Roger Revelle* (RR2107) with AUV *Sentry* and ROV *JASON*, offered a unique opportunity to examine the emission of hydrothermally derived fluids, their buoyant rise, as well as the evolution and fate of the neutrally-buoyant plume in the mid-water. Here, we present the results of a targeted lateral transect using chemical sensors mounted on AUV *Sentry* and a towed rosette, including novel *in situ* methane instruments demonstrated for the first time in the field here. Fig. 5.1 illustrates the overall design of the transect experiment. We show that methane acts as a reliable indicator of hydrothermal activity in the northern Guaymas Basin on a spatial scale of 1.5-3 km at 100-150 m altitude. Methane performed similarly to standard turbidity sensors in this trial (detection 2.2-3.3 km), more sensitively than oxidation reduction potential, and more clearly than temperature, salinity, and oxygen instruments which readily responded to physical mixing in background seawater. We additionally examine the relationships between different sensing modalities, and demonstrate how real-time cross correlative or time-series regime identification could be used to assist in survey design for future exploratory missions.

5.2 MATERIALS AND METHODS

5.2.1 SITE DESCRIPTION

Located in the central Gulf of California (Mexico), the Guaymas Basin is a mid-ocean ridge extensional spreading center system, with the unique characteristic of being heavily overlain with high amounts of organic-rich sediment. While the primary spreading center axis trends southwest to northeast, the axis of the spreading center in the more

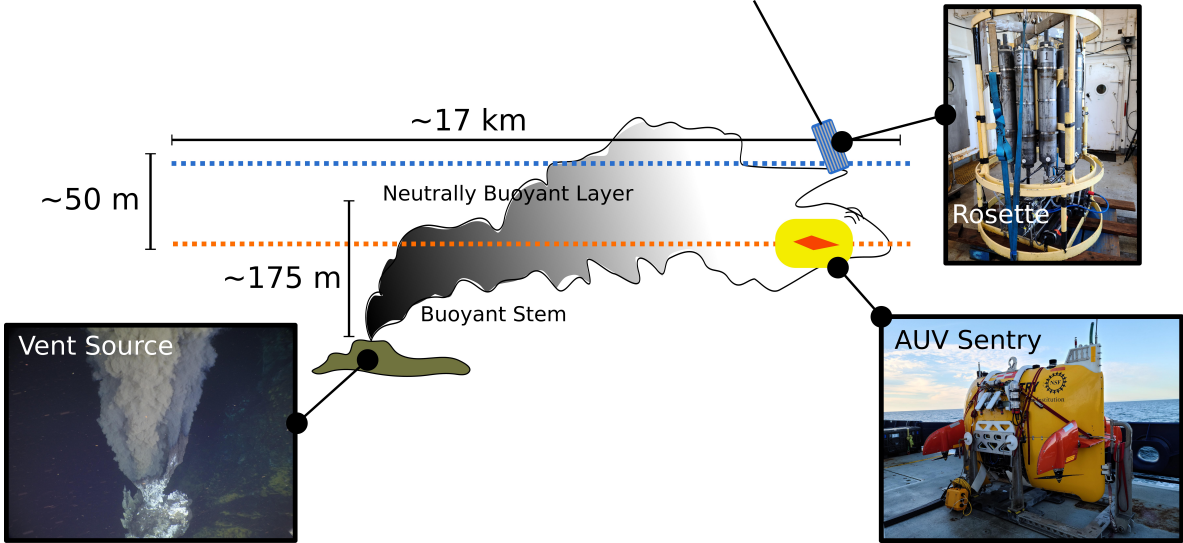


Figure 5.1: Overview of general transect design. Plumes generated by black smoking chimneys at an active hydrothermal ridge in the Northern Guaymas Basin (one example pictured here, taken with an arm mounted MISO camera by ROV *JASON* during RR2107) rise approximately 175 m in the water column and are advected and turbulently mixed with background seawater. AUV *Sentry* and a towed CTD rosette, both equipped with turbidity, oxygen, temperature, salinity, and methane probes, fly trajectories that aim to intersect the lower and upper neutrally buoyant plume layer, respectively. A comparison of the observations collected by both platforms is then used to demonstrate the efficacy of various sensors and algorithmic detection schemes.

well-studied southern end does not extend linearly northeastward, with the northern end of the axis offset to the northwest. The subseafloor eruption and emplacement of lava into the heavy sediment overburden gives rise to a unique set of hydrothermal characteristics. Among these, the geochemical composition of the emergent fluids and volatiles is highly enriched in dissolved organic compounds, carbon dioxide (CO_2), hydrogen (H_2), ammonium (NH_4^+), and methane (CH_4) [21, 22]. While the southern end of the basin has been the subject of a long history of geochemical and biological examination (e.g., [21–25]), hydrothermal activity was only recently documented along the northern end of the basin at a 600 m long ridge located at a depth of 1850 m [26, 27]. Several tall sulfide chimneys 10–25 m in height are located along the ridge, and emit fluids highly-enriched in CO_2 , H_2 , CH_4 among others (Fig. 5.2). The black smoker vents associated with these chimneys consist of clusters of tens of small ($<0.01 \text{ m}^2$) orifices, emitting turbid fluids heated to over 340°C , as observed during RR2107 by ROV *JASON*. In this work, we use the closest identified chimney to the transect trajectories at (27.407489 N, 111.389893 W) as a spatial reference point.

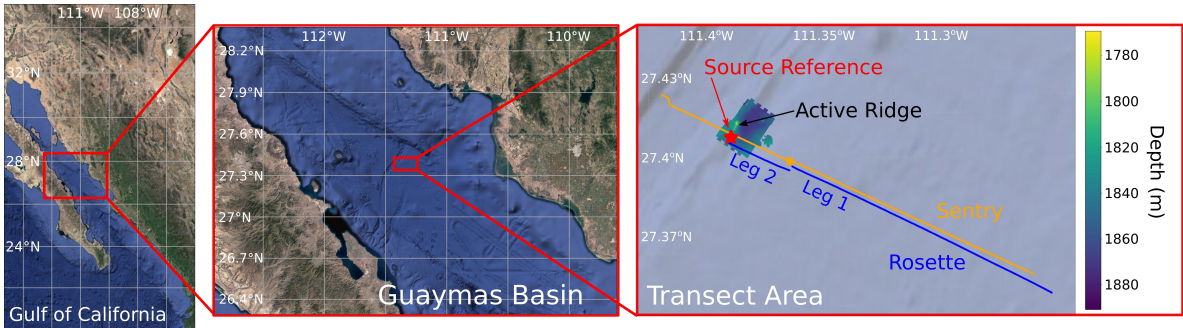


Figure 5.2: AUV *Sentry* and a towed rosette were used to perform coincident several kilometer long trajectories in the Northern Guaymas Basin. The rosette was redeployed mid-trajectory in order to empty the Niskin bottles onboard; this split the rosette trajectory into Leg 1 and Leg 2. The trajectories intersected a region of known hydrothermal activity in the northern basin; a bathymetric relief of this region is overlaid on the far right panel. The red star on the bathymetric relief marks the nearest point of identified hydrothermal activity (black smokers) relative to the trajectories (27.407489 N, 111.389893 W), and is used as a reference point in this work. Imagery is provided by the GoogleTiles API in Cartopy. The bathymetric relief is rendered using data collected by AUV *Sentry* during research cruise RR2107.

5.2.2 SAMPLING PLATFORMS AND INSTRUMENTS

During expedition RR2107, AUV *Sentry* and a towed rosette were deployed to perform a multi-kilometer transect. Two novel *in situ* methane instruments were deployed during the transect, one on *Sentry*, and the other on the towed rosette. Physical water samples collected by the Niskin bottles on the rosette were processed shipboard to measure both methane and ammonium content. To increase the total number of bottle samples that could be collected over the transect, the towed rosette was deployed and recovered twice; we will refer to the rosette transect before the first recovery as “Leg 1” and after re-deployment as “Leg 2.” AUV *Sentry* was placed in a holding pattern when the rosette was on the ship deck to ensure that spatial measurements between the platforms were temporally comparable.

AUV *Sentry*

AUV *Sentry* executes pre-set trajectories (encoded as a set of waypoints) once underway. During this transect, a starting point at (27.345152 N, 111.253108 W) and ending point at (27.460812 N, 111.527694 W) were given, and a holding pattern was programmed to be executed when the rosette was on the ship deck for sample retrieval after Leg 1.

This holding pattern was centered at (27.39592 N, 111.3674 W) and was a lawnmower (back and forth) pattern of approximate dimensions 225 m x 225 m with 15 m resolution. The standard scientific instrumentation deployed on *Sentry* include an oxygen optode (Aanderaa 4330F), an optical backscatter sensor or OBS (Seapoint Turbidity Meter), an oxidation-reduction potential sensor or ORP (NOAA), a CTD (SeaBird SBE49), and 7000 m rated pressure sensor (Paroscientific 8B7000-I). The Pythia instrument (described in Sec. 5.2.2) was additionally installed onto *Sentry* for the transect.

TOWED ROSETTE

During the transect, the rosette was equipped with an ultra-short baseline (USBL) acoustic transceiver to allow the real-time position of the rosette to be tracked with respect to the ship. Scientific instruments mounted on the rosette included a transmissometer (C-Star), a 6000 m rated CTD (SeaBird SBE 911plus), twelve 10 L Niskin sampling bottles, and an oxygen optode (Aanderaa). The SAGE instrument (described in Sec. 5.2.2) was also fixed to the rosette for the transect. Default instrumentation on the rosette was communicated via the winch cable to the rosette watchstander station in the computer lab onboard the ship. Ship speed was set to $\sim 0.5 \text{ m s}^{-1}$ (~ 1 knot) to assist in controlling rosette depth and winch tension. Niskin bottles were fired according to a schedule that favored more bottles near the ridge. A scheduled stop approximately 3 km from the ridge was used to collect samples from twelve full Niskin bottles and re-deploy the rosette to take an additional twelve bottle samples from the stop to the end of the transect.

DISSOLVED METHANE ANALYSIS WITH LASER-BASED SPECTROSCOPY A Los Gatos Research (LGR) Dissolved Gas Extraction Unit (DGEU) and coupled LGR Greenhouse Gas Analyzer (GGA) were used to measure dissolved methane in seawater collected by Niskin sampling bottles fired during the transect. The DGEU uses a membrane contactor for dissolved gas extraction. Extracted gas is then pumped to the GGA which uses off-axis integrated cavity output spectroscopy for making 1 Hz, precise (<2 parts per billion) measurements of methane in the measurement range of 0-1000 ppm. Extraction of gas is imperfect by the DGEU, and so we apply an extraction efficiency correction of 2.3-3.3% (for calibration details, see Appendix A.1). Methane measurements in ppm are subsequently converted to nanomolar (nM) using coincident salinity and temperature measurements observed by the rosette CTD. Calibration of the GGA was completed

using gas standards from Mesa Gas [28]. During the transect, nine of the twelve bottles from Leg 2 were processed using the DGEU and GGA for methane analysis.

AMMONIUM MEASUREMENT Concentrations of ammonium (NH_4^+) were determined onboard within 6 hours of collection from the Niskin bottles following the OPA method [29] in a 1 cm cell using an Aquafuor Field Fluorometer (Turner Designs). Standards were prepared using Milli-Q and surface sea water, and then corrected for matrix effects following [30]. Analytical precision was 5 nM, with a detection limit of 1 nM. Ten of the twelve Niskin bottles were processed in this way during Leg 2 of the rosette transect.

METHANE SENSORS

Two novel sensors for *in situ* methane observation were deployed on the rosette and AUV *Sentry*. The Sensor for Aqueous Gases in the Environment (SAGE) was deployed on the rosette and a real-time cavity ringdown spectrometer called Pythia, was deployed on AUV *Sentry* (Fig. 5.3). Both instruments were in active development during this cruise, and so we report all measurements from these instruments as normalized observations (this can be interpreted as a sensor “saturation” value) in lieu of calibrated concentrations. For the purposes of the analyses herein, there is no loss of generality in the methods proposed to detect hydrothermalism using these normalized values.



Figure 5.3: The SAGE and Pythia instruments mounted on the rosette and AUV *Sentry*, respectively.

SAGE SAGE is a dissolved gas sensing technology developed at the Woods Hole Oceanographic Institution (WHOI), and this expedition served as the first at-sea vali-

dation of the sensor's operation. SAGE technology has been previously described in [31, 32]. Briefly, SAGE is based on infrared absorption spectroscopy performed on extracted gas from seawater via a gas permeable (and water impermeable) membrane. Once the gas enters the sensor, it fills a hollow-core optical fiber (HCF) which also guides light from a laser source tuned to measure the gas species of interest. The amount of target gas present is determined by measuring the amount of light absorption through the HCF using a photodetector. This prototype version of SAGE was configured to measure methane in the range of 0-10,000 ppm. The resolution of the sensor is <1 ppm. The response time for the deployed configuration was approximately 12 minutes, and the instrument was minimally sensitive to temperature for the scales shown in this paper, (i.e., <2% of the full scale of the observed signal). SAGE is 5.5" long with a 9" outer diameter, and the power requirement was 7 W during this field deployment.

PYTHIA Pythia is a novel deep-sea methane sensor developed utilizing real-time cavity ringdown spectroscopy (rt-CRDS) developed by WHOI [33] and Ring-IR Inc. [34], and capable of operating to 4000 m depths. Pythia extracts dissolved gas from sea water using a large (113 cm^2) surface area membrane. The extracted sample gas enters an optical cell where it is interrogated by a pulsed mid-infrared Quantum cascade laser (QCL). The laser light is absorbed by methane present in the cell, and the concentration of methane is determined by monitoring the pulsed ringdown signal from the cell using a mercury cadmium telluride (MCT) detector. While the response time of the sensor is slow, on the order of 35 minutes, the sensor is responsive to small (<2 ppm) changes in methane; the temperature sensitivity of Pythia has not yet been characterized. Pythia is ideally suited for long dives in environments in which changes to the methane concentration vary over long temporal and spatial scales. Details on the process for normalizing Pythia observations (which are strongly nonlinear and additionally require time correction) are provided in Appendix A.3. Pythia is 24" long with a 4.5" outer diameter, and was operated at a power range between 30-50 W during this field deployment.

5.2.3 ANALYTICAL PROCEDURE

Observations collected by sensors deployed on AUV *Sentry*, including Pythia, were merged into a single dataframe using a common 1 Hz time reference; data were linearly interpolated onto this common time reference if they did not share an exact timestamp. With the exception of the derivative of ORP signal, all data for the purposes of

visualization is smoothed using a centered rolling average over 5 minute intervals. Additionally, temperature, oxygen, and salinity measurements are normalized with respect to depth (as these quantities are anticipated to be functions of depth in the weakly stratified deep waters). Depth correction is performed by fitting a linear function to the average observation collected in 20 m wide depth-bins, and computing the residuals of all data points with respect to this line (see Appendix A.4 for plots of the linear functions). Rosette data is treated in the same fashion as *Sentry* data. Down-cast and up-casts are removed from both *Sentry* and rosette data streams for all visualizations.

5.2.4 TRANSECT DESIGN AND EXECUTION

AUV *Sentry* and the rosette were deployed in the basin approximately 16 km from the northern hydrothermal ridge structure, at (27.348152 N, 111.253108 W) with a course of 295° set to intersect the southern part of the ridge (Fig. 5.2). The *Sentry* trackline was placed approximately 200-300 m north of the rosette to avoid any risk of entanglement. *Sentry* was set in altitude hold mode, targeting 120 m from the bottom (this places *Sentry* at a depth of approximately 1750-1700 m, and at the top of its altitude-hold range). Rosette depth was targeted to be approximately 1650-1600 m, controlled primarily by the speed of the ship and length of the winch cable. These depths were designed based on an estimated model of the neutrally buoyant plume layer, as described in Sec. 5.2.4. Leg 1 of the rosette trajectory was terminated at a planned stop at (27.393855 N, 111.364637 W), and Leg 2 was resumed at (27.460812 N, 111.527694 W); see Appendix A.2 for the schedule of bottle samples collected during Leg 2 presented in this manuscript. At the time of the transect, there were no known hydrothermal sites present over the sampling trajectory, save for the northern ridge. Hydrothermal vents in the southern basin were located approximately 40 km further south from the transect starting location [24].

MODELING TO INFORM TRANSECT DESIGN

The selection of heights for the rosette and AUV *Sentry* was informed by a simple buoyancy model of expected plume characteristics on the ridge, and known operational constraints of AUV *Sentry* (i.e., an absolute floor and ceiling of operation above the bottom). Using an adapted plume crossflow model developed by [35] (see Appendix A.5 for more detailed information) with a nominal current crossflow value of 0.1 m s^{-1} , vent temperature of 340°C , and estimated background seawater stratification as per [18],

we hypothesized that a neutrally-buoyant layer may form between 1570 m and 1750 m. We selected the depths for the rosette (1600-1650 m) and AUV *Sentry* (1700-1750 m) given this information in order to target both the upper and lower estimated neutrally buoyant layer (NBL), respectively. We targeted the NBL to increase the likelihood of intersecting plume waters during the transect over a broad, multi-kilometer scope. This is in contrast with targeting the plume buoyant stem, which though significantly easier to distinguish from background seawater, may only have an expression on the order of several square meters.

REAL-TIME DATA FEEDBACK AND WATCHSTANDING

During the transect, data from the standard rosette sensors were available in near-real time at the watchstander station in the shipboard computer lab. This allowed watchstanders to monitor the depth of the rosette and relay requests to the winch operator on deck, and display the data on live-updating visualizers. AUV *Sentry* relayed occasional data packets up to 128 bytes in length at a rate of approximately 0.01 Hz. These data packets were subsequently graphed on a computer monitor that was linked to the *Sentry* network. A total of 600 messages with information about the standard science instruments on *Sentry*, and 583 messages with information from the Pythia instrument were transferred during the transect.

5.3 RESULTS

5.3.1 METHANE OBSERVATIONS FROM SPECTROSCOPIC INSTRUMENTS

Elevated methane was observed over a spatial scale of several kilometers, significantly rising as both AUV *Sentry* and the rosette approached the source of known hydrothermalism on the transect (Fig. 5.4). As both methane instruments used on this cruise were in active development, we report methane observations as normalized values from 0 to 1. We use a normalized value of 0.5 as a conservative threshold for classifying elevated methane measurements. Pythia, mounted on *Sentry*, reached and exceeded this threshold for elevated methane starting at approximately 3 km from the hydrothermal reference point at (27.407489 N, 111.389893 W); SAGE, flying nearly 50 m higher in the water column, reached this threshold starting 1.5 km away. For a less conservative threshold (0.3), these spatial detection points are reached 6.8 km and 2.2 km away,

respectively. SAGE observed a sharp peak of methane just under 1 km from the reference source, with rapid decline of observable methane soon after. In contrast, Pythia reached a methane peak essentially at the 0 km reference point, and shows a gradual decline in methane as *Sentry* descends into a graben just north of the hydrothermal ridge; the rosette was pulled from the water at the ridge. The difference in spatial detection patterns indicated by these instruments may be a function of both the different sensor modalities/sensitivities, and the natural structure of the neutrally-buoyant layer and the relative position of the two platforms within it.

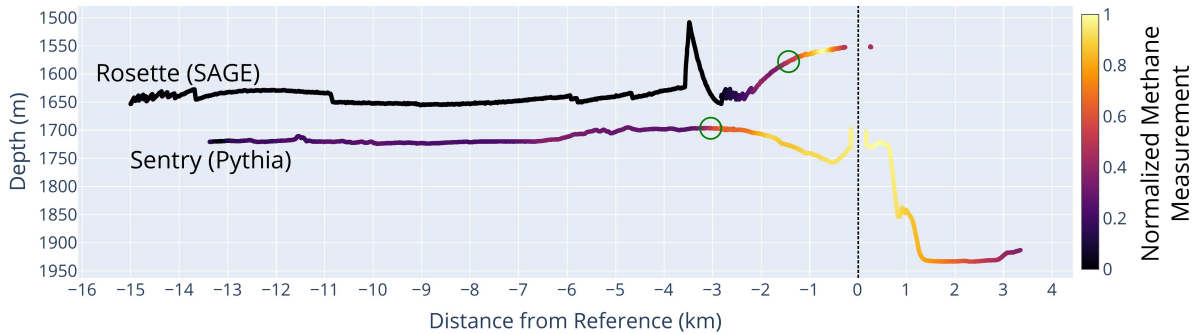


Figure 5.4: Normalized methane values observed with both SAGE (rosette) and Pythia (*Sentry*) over reference distance from (27.407489 N, 111.389893 W). The transect begins at the left of the plot and proceeds to the right. Strong methane anomalies, defined as points above a conservative threshold of 0.5 normalized values, are present starting 3 km from the reference source as observed by Pythia, and 1.5 km as observed by SAGE (open green circles).

5.3.2 METHANE AND AMMONIUM OBSERVATIONS WITH THE ROSETTE

Ammonium is a microbial energy source and reduced compound that is produced by the hydrothermal vents at Guaymas Basin. It is expected that ammonium and methane behavior in the basin will behave similarly, providing a “check” on the methane trends we observe in methane bottle samples, and recorded by SAGE. Focusing primarily on Leg 2 of the rosette transect, we observed a correspondence between methane and ammonium elevation in the approach to the hydrothermal ridge (Fig. 5.5). Methane samples processed directly from Niskin bottles as outlined in Sec. 5.2.2 show a peak methane concentration of 3000-4000 nM (this range is associated with the extremes of calibrated extraction efficiencies valid for the equipment used), approximately 0.75 km

from the hydrothermal reference point. Ammonium tracks closely with methane, at 3-4 times smaller concentration, reaching a peak of approximately 1000 nM.

Normalized methane observations by SAGE generally follow the trends shown by the bottle samples, similarly showing a spatial peak at 0.75 km. However, by its nature, SAGE yields a significantly more resolved signal; a small, secondary peak is observed by SAGE at 2 km from the reference point which is essentially missed by the bottle samples. Additionally, by virtue of operating continuously, there is no need for human interaction (unlike for processing bottle samples, which can require time-intensive *ex situ* analysis).

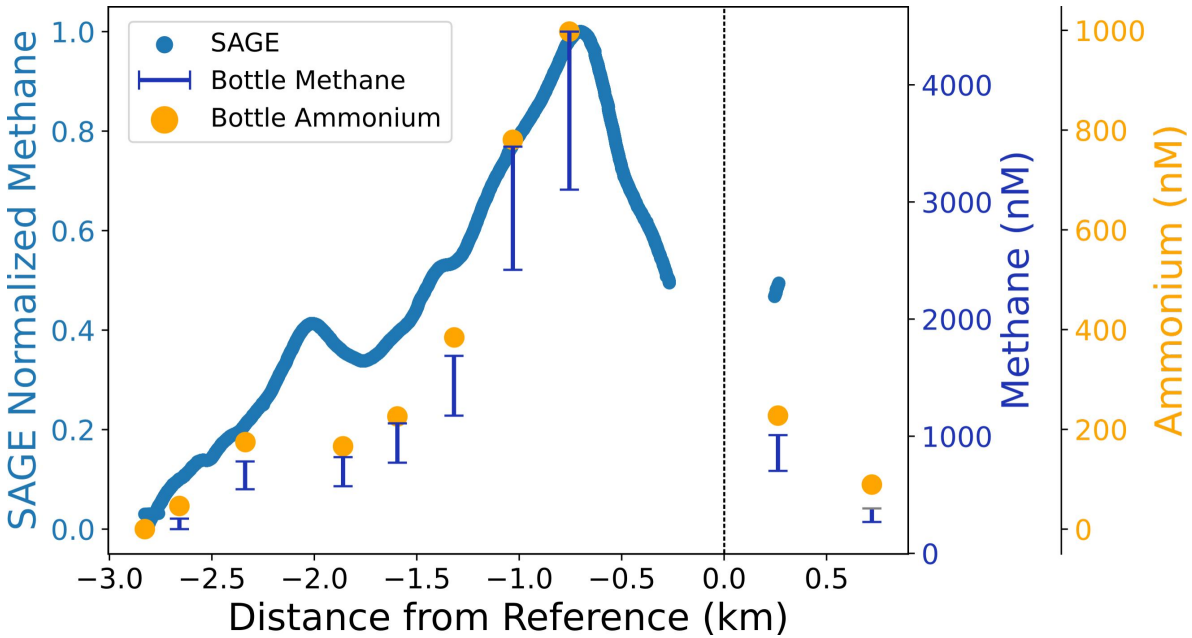


Figure 5.5: Normalized methane measurements by SAGE plotted with methane measurements taken from Niskin bottle samples (as measured by DGEU/GGA equipment) and ammonium measurements. Bottle methane measurements are reported as a range to reflect sensitivity of the measurement procedure to a calibrated extraction efficiency. All measurements trend towards a peak observation of methane and ammonium 0.75 km from the reference source. SAGE additionally observes a secondary peak approximately 2 km from the source, which is essentially missed by the bottle sample schedule.

5.3.3 TURBIDITY

Turbidity is a commonly used indicator for detecting hydrothermalism from smoking vents; particulate matter produced by smoking vents can remain suspended in the neutrally buoyant layer, acting as a non-conservative tracer for hydrothermalism (e.g., [36]).

In the Guaymas Basin, suspended particulates have been shown to be composed of metals like iron, aluminum, and manganese [13] and are primarily mixed into bottom waters from hydrothermal activity. We report turbidity measurements as normalized values to make direct comparison between the platforms; in absolute terms, the transmissometer on the rosette reported beam attenuation values between 0-0.2 and the OBS on *Sentry* observed backscatter values between 0.08-0.14. The OBS on *Sentry* encountered an error from the beginning of the dive, potentially caused by a persistent air bubble, until approximately 4.5 km from the ridge reference point; we therefore do not report these early measurements.

We observed elevated turbidity (defined by a conservative threshold of 0.5 in the normalized data) with the transmissometer on the rosette starting approximately 2.2 km from the reference source and 3.3 km with the OBS on *Sentry* (Fig. 5.6). Even with a less conservative threshold (0.3) these detection points only slightly improve to 2.5 km and 3.4 km respectively. With *Sentry*, we observe a rapid decline in turbidity within tens of meters west of the source reference (positive distance in Fig. 5.6). This may be indicative of the direction of prevailing crossflow (southeast) in the basin, which would directionally bend a buoyant plume stem and advect the neutrally buoyant layer.

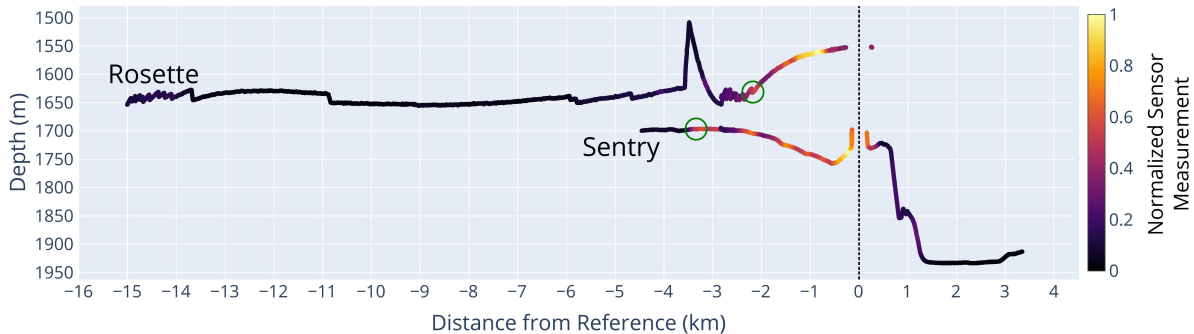


Figure 5.6: Turbidity observed as beam attenuation on the rosette transmissometer and optical backscatter on AUV *Sentry* instruments. *Sentry* encountered a sensor error until approximately 4.5 km from the ridge reference point. After this point, elevated turbidity is detectable throughout the dive, with significant elevations within 3.3 km east of the ridge reference point, dissipating within tens of meters to the west. Elevated turbidity is observed by the rosette 2.2 km from the ridge reference point to the east.

5.3.4 OXIDATION REDUCTION POTENTIAL

AUV *Sentry* carries an ORP sensor; there was no comparable sensor on the rosette. ORP sensors are commonly used in hydrothermal plume hunting, and can be a strong

indicator of recently emitted hydrothermal fluids. The derivative of ORP (noted here as $d\text{ORP}/dt$) is particularly used, in which negative $d\text{ORP}/dt$ values typically indicate transition from background water into hydrothermal fluid. During the transect, only one significant $d\text{ORP}/dt$ deviation was observed, within 200 m from the ridge reference point (Fig. 5.7).

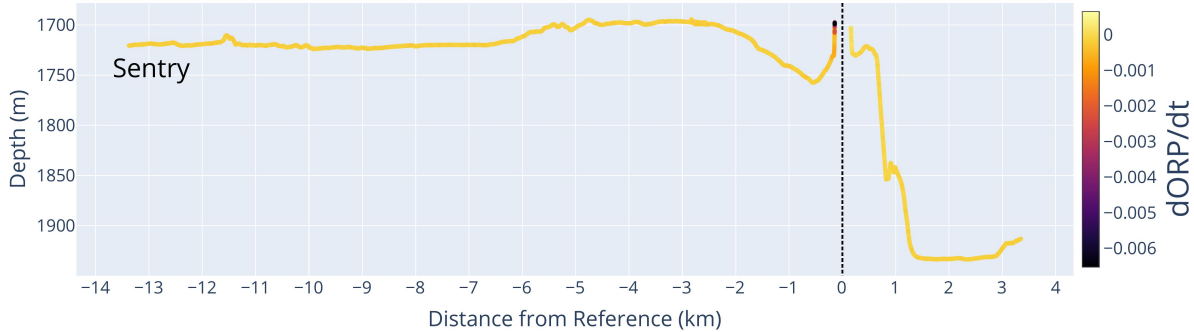


Figure 5.7: The derivative of ORP observed by data collected on AUV *Sentry*. Negative slopes are indicative of entering hydrothermal fluids. Only one region of the transect demonstrated a significant reaction to ORP, within 200 m of the reference point.

5.3.5 TEMPERATURE, SALINITY, AND OXYGEN

Temperature, salinity, and oxygen are expected to be weakly stratified in deep ocean waters, however fluids from hydrothermalism should register as anomalies when present. The magnitude of valid anomalies (i.e., anomalies that positively identify fluids impacted by hydrothermalism) can be exceedingly small; temperature at a vent can be hundreds of degrees Celsius, but anomalies in the water column on the spatial order of only 10 m can be measured as single degrees, and within a nonbuoyant plume on the order of hundreds of meters from the source, only register a few hundredths of a degree [37].

We compute temperature, salinity, and oxygen anomalies according to the process described in Sec. 5.2.3 and show the results in Fig. 5.8. Salinity anomalies, although apparently coherent, are reported within the empirical sensor noise for the CTD instruments on both the rosette and *Sentry*. Temperature anomalies on the scale of hundredths of a degree are observed throughout the transect, with two key regions of high temperature anomaly, one located 6-12 km from the reference source, and the other within 3 km of the source. Both the rosette and *Sentry* observe these regions; with *Sentry* observing the first anomaly in a narrower margin between 8-11 km from the reference source. The first region of positive temperature anomaly closely corresponds

with marginally fresher water; whereas the region of higher temperature anomaly near the source is not consistently matched in temperature (the rosette observes more salinity content, whereas *Sentry* observes neutral or slightly less salinity content). Oxygen is reported as nominal or slightly depleted within the regions of notable temperature and salinity anomaly.

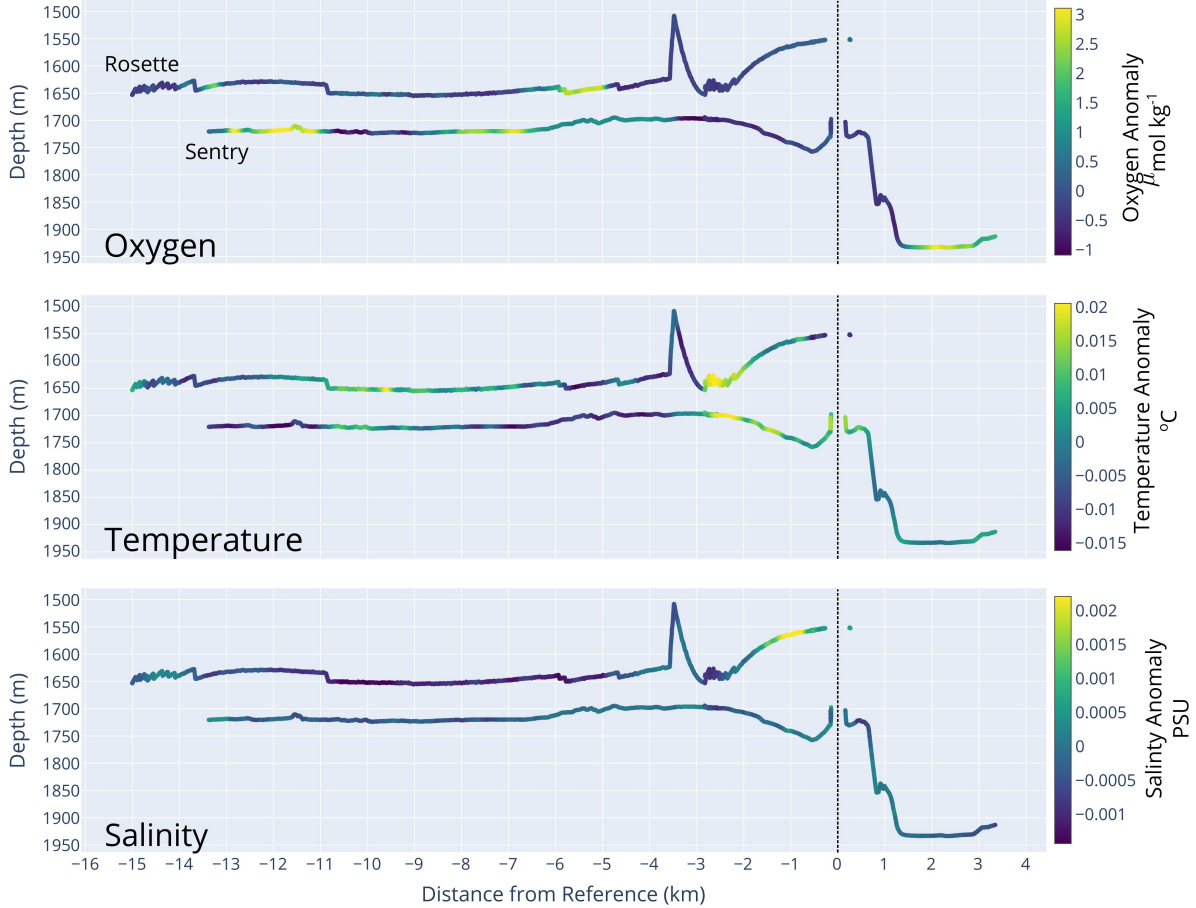


Figure 5.8: Depth-corrected oxygen, temperature, and salinity over reference distance. Two notable regions of high temperature deviation from expected temperature are observed between 6-12 km (rosette; 8-11 km by *Sentry*) and within 3 km of the reference source. The first region of temperature anomaly is closely matched with fresher salinity measurements; whereas salinity is measured as marginally higher near the reference source by the rosette CTD and nominal or lower by the *Sentry* CTD. In both regions, oxygen is nominal or slightly depleted, with regions of notably elevated oxygen at the boundary of these regions.

The first region of interest, far afield from the plume reference point, appears coherent and has similar detection qualities to the near-reference region; however, given the typical expectation of temperature dissipation from hydrothermal sources, it would be surprising if this first region were connected with hydrothermalism. The shape of the

warm, slightly fresher and oxygen depleted intrusion (laterally broad higher in the water column, and appearing to narrow based on the observations taken by the rosette and *Sentry* approximately 50 m offset in altitude) also does not follow expected patterns in a neutrally buoyant plume layer. Lack of significant methane and turbidity observations in this same region, as presented in Sec. 5.3.1 and Sec. 5.3.3 respectively, additionally casts doubt on hydrothermalism as a driver for this anomaly. Water mass mixing between the bottom waters, largely sourced from Pacific Deep Waters and the Pacific Intermediate Waters [38] may be an alternative explanation, but is out of scope for this paper to investigate.

5.4 DISCUSSION

5.4.1 SENSOR CROSS-CORRELATIONS

Successfully detecting hydrothermalism in the deep ocean is a significant challenge, and detection may be most effective using a combination and corroboration of anomalies across multiple sensor inputs (e.g., [39]). Here, we examine the cross-correlation between sensors mounted on each of the platforms. Both a global and rolling Pearson correlation coefficient was computed, showing respectively overall correlation trends, and situation dependent correlation.

Fig. 5.9 shows the global correlation among sensors mounted on the rosette individually over Leg 1 and Leg 2, in addition to sensors mounted on *Sentry*. In the absence of significant geochemical features in a target environment, it is expected that no or only weak correlation will be computed globally, as individual sensor noise (which is independent) will dominate the computation; when geochemical structure is present in the environment, it is expected that weak to strong global correlation will be computed as the environment is imposing a (shared) signal across at least a subset of sensors. This is well illustrated by the cross-correlation matrices for the rosette legs, with global coefficients for Leg 1 reporting no correlation between sensors save for a slightly negative correlation between temperature and oxygen, and for Leg 2 reporting weak to strong correlations between all sensors, with notably strong positive correlation between turbidity and methane. Interestingly, in Leg 2 a negative correlation is reported between temperature and methane, and a positive correlation is measured between methane and oxygen measurements. This runs directly counter to expectations; and also counter with the relationships observed by *Sentry* which marks relationships between methane and

temperature as positively correlated, and between methane and oxygen as negatively correlated.

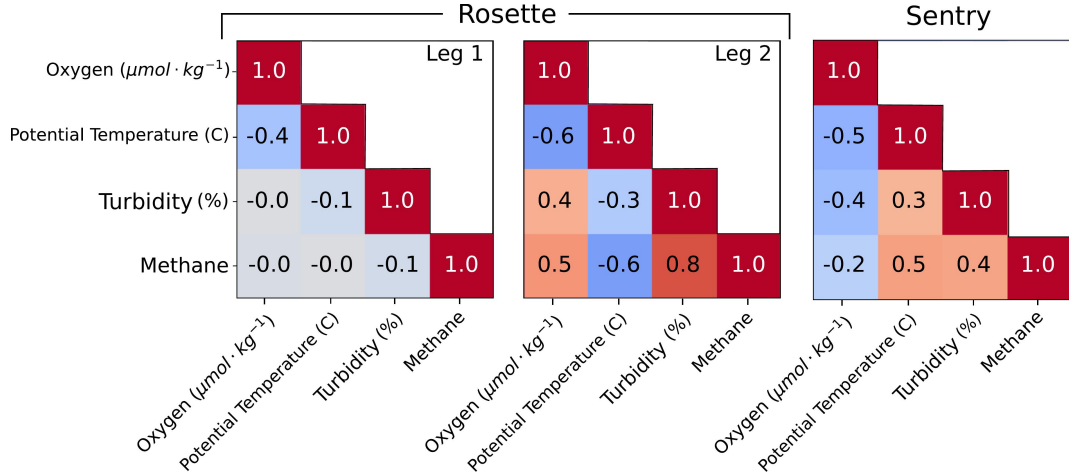


Figure 5.9: Global Pearson correlation coefficient between sensors mounted on the rosette and *Sentry*. Correlation differences between Leg 1 (far from the reference point) and Leg 2 (near the reference point) are indicative of different sensor correlation behaviors with respect to ambient seawater conditions and hydrothermal fluid interception. *Sentry* correlation coefficients reflect an expected relationship between temperature and methane (positive), methane and oxygen (negative), and turbidity and methane (positive) that may be stereotypically associated with hydrothermal fluids. In contrast, the Leg 2 rosette correlation factors do not meet this expectation, despite showing strong overall correlative structure.

The difference between correlative behaviors between the rosette legs, and also between the platforms generally, motivates a finer study of correlation. Fig. 5.10 shows a rolling correlation coefficient computed over a window of 30 minutes for the rosette. Computing local cross-correlations with respect to time, rather than distance, is mathematically more sound, and also aligns directly with how cross-correlative monitoring may be used during live exploration missions. With respect to the rosette, we observe that in Leg 1, nominal correlation is weak or non-existent between most sensors, with exception for oxygen and temperature. We can additionally see that the correlative “micro-structure” of the local window shows regions of possible interest that are greater than nominal – for instance, measurements taken between 03:00-05:00 show a coherent region of negative correlation between temperature and turbidity, and positive correlation between temperature and oxygen. Similarly, around 02:00 a region of strong positive correlation between oxygen and temperature is observed. In Leg 2, we see overall more strong, pronounced correlations between sensors, with a distinct period centered in the hour around 10:00 in which correlation between temperature and

methane, temperature and turbidity, oxygen and methane, and oxygen and turbidity appear to “flip” compared to the periods of time directly before and after this period, potentially indicating a significant anomalous feature. This time period is well aligned with the spatial proximity of the rosette with the reference source.

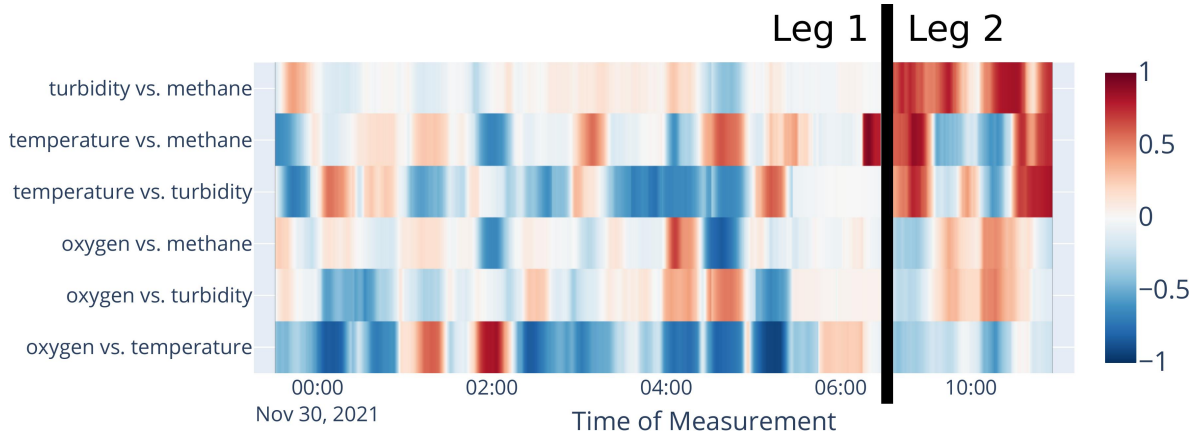


Figure 5.10: Local (rolling) Pearson correlation coefficients between sensors mounted on the rosette over 30 minute windows.

Local correlation trends during the *Sentry* transect are reported in Fig. 5.11, and show an intense relationship between oxygen and temperature throughout the dive, with most regions reporting a strong negative correlation, both with two regions showing positive correlation between 07:00-08:00 and again at 11:00. This strong relationship is also reflected in the relationships of temperature and oxygen with methane, being nearly correlative mirrors with respect to methane. During periods in which the turbidity sensor was operational, a gradual correlative “flip” and intensity increase around the 11:00 sampling time may indicate a structured water mass. This time agrees with the spatial proximity of *Sentry* with the reference source.

Correlation alone is not sufficient evidence for the presence of hydrothermal fluids. For instance, some of the coherent regions of positive or negative correlation with methane any time during Leg 1, or early in the *Sentry* transect, are misleading, as the overall methane content of the water was exceedingly small or essentially background. Rolling correlations, coupled with absolute thresholds as reported in this results section, may together be useful tools for indicating transition into new water masses, their absolute properties of which could be used to more closely classify the types of water masses. This correlative study also demonstrates that correlations in expectation (e.g., temperature and methane being positively correlated in hydrothermal fluid) may be reductive assumptions of the complexities of plume evolution within a water column, supporting

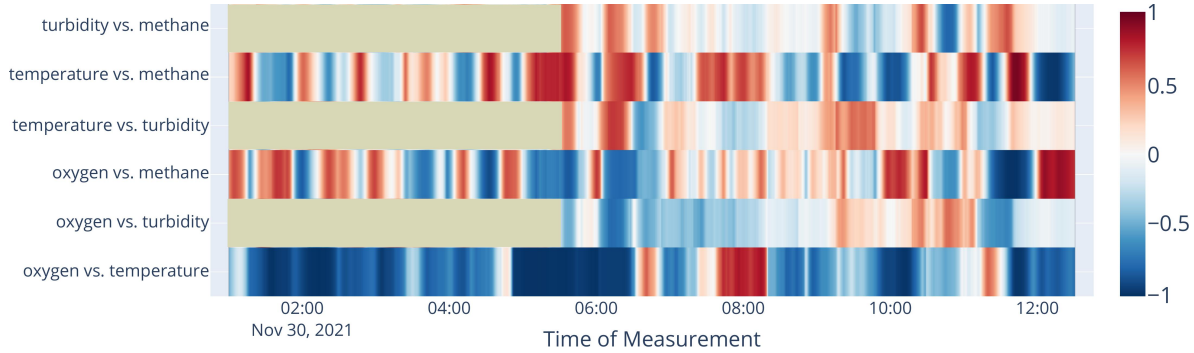


Figure 5.11: Local (rolling) Pearson correlation coefficient between sensors mounted on AUV *Sentry* over 30 minute windows.

similar findings by, e.g., [40]. For instance, aging plume waters in the neutrally buoyant layer may long have settled to a temperature indistinguishable from background, but still be particulate and possibly gas rich. This motivates additional study of the “classes” of hydrothermal fluids and their classifying characteristics, which could in turn be used to support studies of microbial evolution and nutrient consumption in plume fluids, or sediment and particulate transport modeling.

5.4.2 HYDROTHERMALISM DETECTION VIA TIME-SERIES REGIMES

As indicated by Sec. 5.4.1, changes in correlative *structure* may be a more useful signal than absolute correlation alone. This notion can be codified as regime changes, which detect inflection points in which a series of observations collected in time may change in typical value, oscillation frequency, or pattern. Here, we compute regime changes using a 30 minute detection window using the `ruptures` Python library and a radial basis function detection kernel, and report regimes using alternating red and blue color blocks in the included figures.

In Fig. 5.12 we show uniquely identified regimes across the entire rosette transect over multiple sensors. We observe that the water-mixing anomaly that occurs early in the transect (Sec. 5.3.5) appears to be detected as regime changes in potential temperature, oxygen, and even a correspondence in lowered beam attenuation. Similarly, regime changes in turbidity and methane are early indicators of significant elevation of both of these factors as the rosette intersects with hydrothermal fluids. Interestingly, a regime change in oxygen and temperature is evident immediately following the first small peak in methane and turbidity. These peaks, in addition to these regime changes, may together be indicative of mixing plume sources from other hydrothermal vents located

along the ridge (that must travel further than fluids from our reference point) or the mixing of ageing plume waters with more recently emitted fluids.

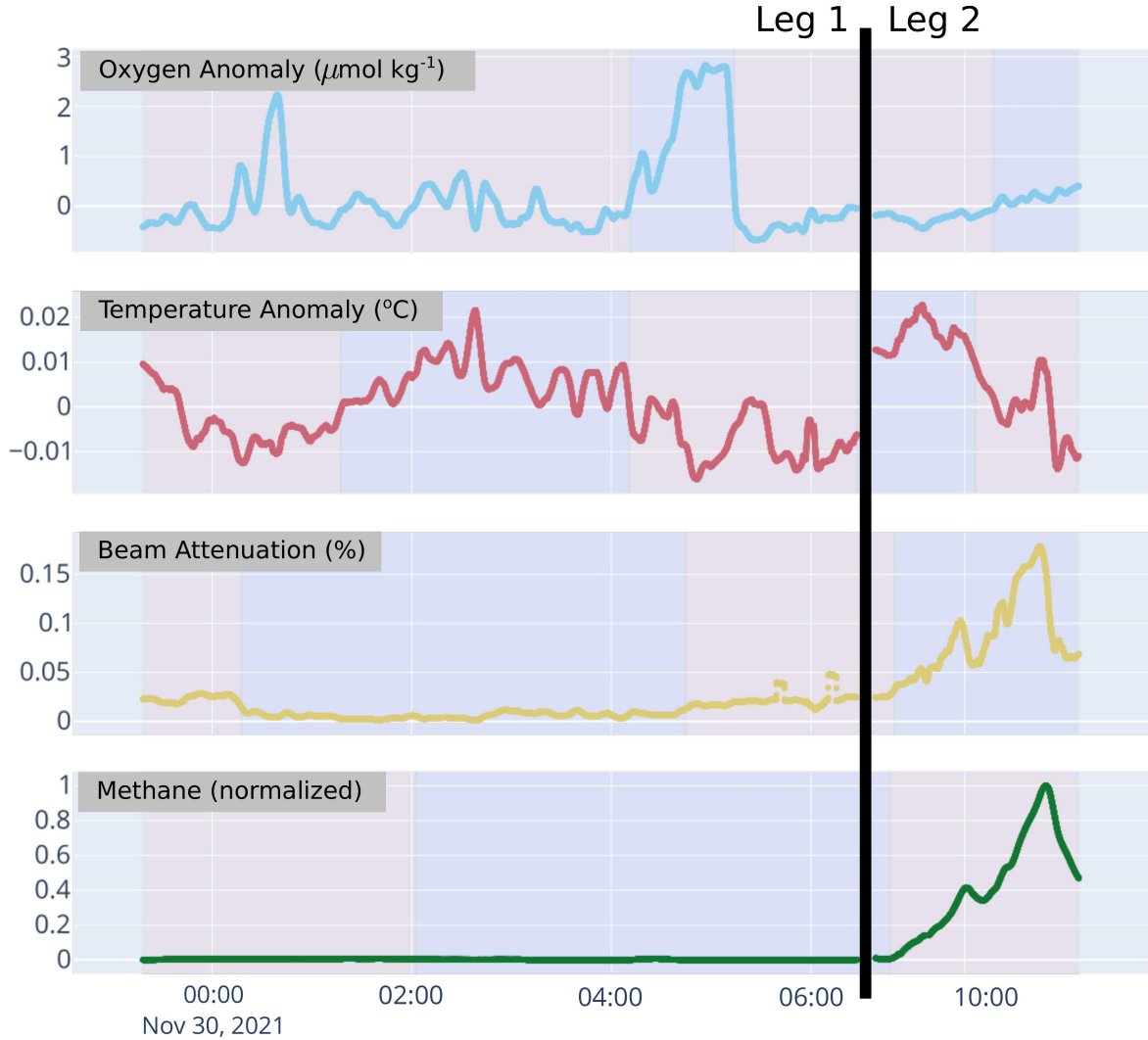


Figure 5.12: Regimes, indicated as alternating blue and red regions, detected during the rosette transect with a 30 minute detection window.

With instruments mounted on *Sentry*, in Fig. 5.13 we see clear “steps” of methane observed by Pythia each marked as a regime. Some of these steps are nearly coincident with regime changes in turbidity, temperature, and oxygen (particularly the steps at 06:30 and 09:30).

Regimes can be mathematically identified in streaming data, making this a potentially useful method to adopt for real-time hydrothermalism discovery. Coupled with absolute measurements by sensing instruments and rolling correlative structure, identifying water masses across multiple data streams can be done live from streaming

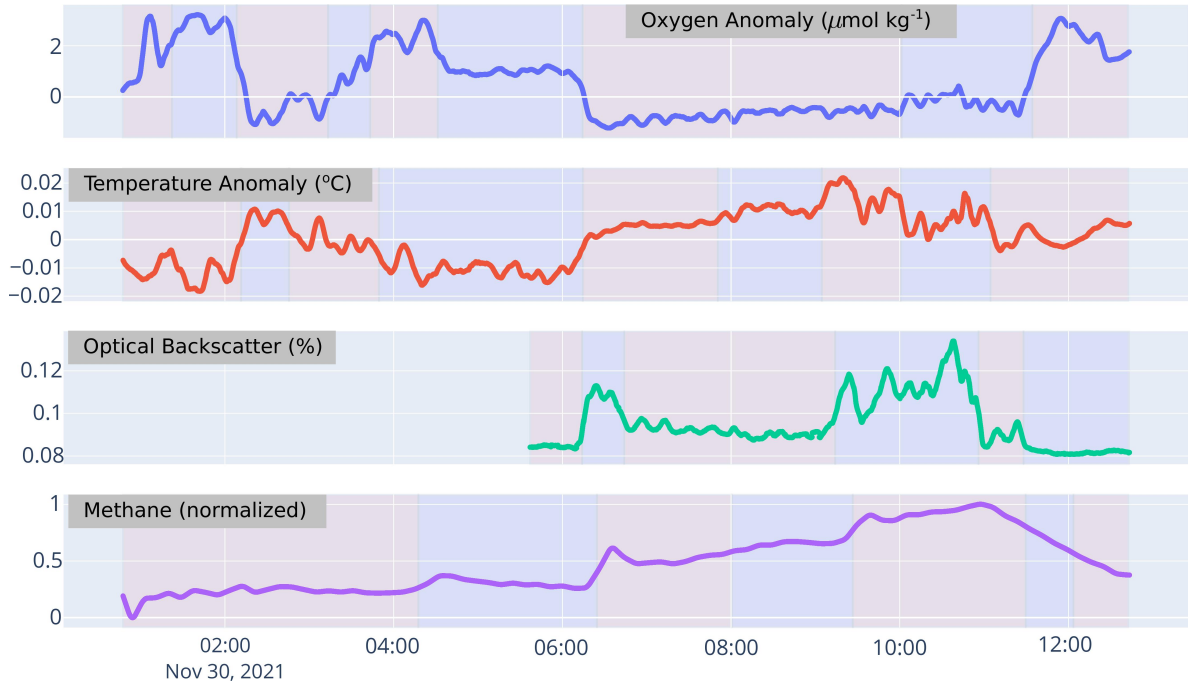


Figure 5.13: Regimes, indicated as alternating blue and red regions, detected during the AUV *Sentry* transect with a 30 minute detection window.

data on the ship, or computed/estimated directly onboard an AUV computer and reported back to watchstanders remotely under data-limited transmission protocols (e.g., acoustic pings).

5.4.3 METHANE IN DEEP SEA EXPLORATION

AUV and sensor deployments during expedition RR2107 served as an initial proving ground for the SAGE and Pythia *in situ* methane instruments for deep sea exploration, and the utility of methane as a potential tracer for hydrothermalism discovery. We showed that, during this transect, both instruments observed significantly elevated methane over a span of several kilometers from a known hydrothermal source in Guaymas Basin. Methane proved to be a strong predictor for hydrothermalism that was not easily confounded by physical oceanographic events (e.g., mixing), giving it an advantage over oxygen, temperature, and salinity. Indeed, in this trial, each of the oxygen, temperature, and salinity instruments were impacted by an unknown physical feature not driven by hydrothermalism, but registered as similar scales of expected anomaly. Methane was also shown to be more expressive than ORP, which only registered a possible anomaly long after significant methane measurements were observed. Turbidity was

a similarly useful and expressive feature of hydrothermalism in this basin, with similar detection scales to methane during this transect. Notably, for less strict detection criteria (i.e., thresholds) on detection, methane significantly outperformed turbidity in terms of detection scale (positive identification up to 6.8 km away, in contrast to 3.4 km for turbidity). Turbidity and methane together make for a strong pairing for hydrothermalism discovery. While neither one alone is a "universal" proxy for hydrothermal activity—not all hydrothermalism of interest produces particulate heavy smoke (i.e., diffuse flow fields) nor do all vents produce significantly elevated methane—they are complementary indicators which can assist in deep sea exploration for anomalous water masses derived from hydrothermalism.

Collecting high resolution measurements of methane during this transect highlighted the rich structure of dissolved gasses in a neutrally buoyant plume layer over multiple kilometers, with multiple peak detections being possibly indicative of mixing novel and ageing hydrothermal fluids, the contribution of multiple sources of hydrothermalism, or complicated internal mixing causing spatiotemporal multimodal distributions of dissolved gas "pockets" throughout the layer. Bottle samples collected on the cruise verified the presence and general trend of methane observed by the instruments, but failed to resolve several features that may be of scientific interest. This motivates the use of *in situ* methane sensors for future studies of hydrothermal fluids in the water column.

5.4.4 ENABLING BETTER DECISION-MAKING FOR HYDROTHERMALISM DISCOVERY

Enabling the interpretation of real-time sensor data and adapting scientific missions accordingly are critical future skills for scientific expeditions and exploration in the deep sea. In preparation for this transect, we utilized a simple physical model to inform the design of the trajectory and monitored progress with live data displays for both the rosette and AUV *Sentry*. While real-time data display for rosettes is now considered standard for oceanographic research, streaming capabilities of scientific data from autonomous platforms like *Sentry* is a relatively new capability. This display infrastructure enabled the science team to make note of the OBS sensor error on *Sentry* while performing the transect, caught a power and logging failure of the Pythia logger upon deployment (which, if left unresolved, would have meant an absence of all methane data associated with *Sentry* for this analysis), and allowed real-time control and decision-

making about the rosette positioning and bottle firing possible. While data presented here was analyzed after the mission, several of these analyses, including rolling correlation and regime detection, could be performed from streaming observations. As a whole, the techniques in this paper present an opportunity for advancing technical infrastructure on a research vessel in order to enhance decision-making capabilities of the science party and engineering teams, both logistically to better diagnose instrument operation *in situ* and scientifically to enhance data collection.

Real-time data collection and processing could have further implications for embodied intelligence as a tool for scientific expeditions. Using models, inference methods, and streaming data, autonomous agents like AUV *Sentry* could be made capable of performing adaptive decision-making for sample collection. Hydrothermalism discovery has long been a motivating use case for intelligent autonomy at sea (e.g., [37, 39, 41, 42]). This transect experiment demonstrates the utility of simple models for tractable, intelligent planning, motivates the possibility of using methane as an additional, reliable data source for performing autonomous behaviors (e.g., adaptive sampling, tracking), and presents the opportunity to embed simple analytical methods for classifying hydrothermal fluids from sensor streams. Being able to not only estimate and map the source of hydrothermal plumes, but to also chart the evolving nature of fluids in the mid-water, would enable an advancement of scientific inquiries that could be pursued with respect to hydrothermalism in the deep ocean. Such queries include the detailed structure of multiple-source plume collision, directly measuring *in situ* the 4D structure of mixing in neutrally buoyant plumes and buoyant plume stems, assessing biological activity supported by plume fluids, tracing the fate of dissolved gasses, and more. We have shown that detection of hydrothermal sources is possible on the scale of several kilometers even in this relatively small basin, and have taken some initial steps to demonstrate core data infrastructure that can improve human decision-making in hydrothermalism discovery; future work and engagement will be focused on advancing these tools to enable the next generation of scientific inquiry in the deep ocean.

6 PHYSICALLY-INFORMED OPERATIONAL ROBOTIC TRAJECTORIES FOR SCIENTIFIC EXPEDITIONS

[TODO: short premise here that also highlights publications]

6.1 INTRODUCTION

Transient, dynamic phenomena—deep-sea hydrothermal plumes, algal blooms, warm core eddies, lava flows—are of interest in many disciplines of observational science. *Expeditionary science* encapsulates the observational sciences that require *in situ* sample collection of environmental phenomena for scientific discovery and model development. In such cases, the environmental targets are typically impossible to observe using remote sensing (e.g., satellites) either due to desired spatial and temporal resolution, environment adversity (e.g., the deep sea, within closed structures), or the nature of the scientific target of interest and corresponding sensing equipment (e.g., building a taxonomy of algae requires physically processing water samples). Expeditionary science is, by definition, conducted in a partially-observable environment, and creating comprehensive pictures of these environments is further complicated by spatiotemporal distributions of dynamic phenomena.

In this article, we study robot autonomy for charting deep-sea hydrothermal plumes, a particular class of scientific spatiotemporal phenomena. Understanding the fate of chemicals and particulates in hydrothermal plumes is of significant interest to biogeochemists and physical oceanographers; however, directly studying plumes in the water column is a substantial challenge. Hydrothermal plumes are driven by density differences between super-heated fluid at seafloor geothermal vents and the cold background

seawater, creating a buoyancy force that causes the vent fluids to rise. The plume is typically chemical and particulate rich, and while rising through the water column, mixes (entrains) with the background seawater until it reaches a point of neutral buoyancy with the ambient seawater. At the neutrally-buoyant layer, fluid from the plume spreads out in a large plane (following an isopycnal of constant density). From this layer, metals, sediment, and other suspended particulates carried by the plume may drop out and be redeposited onto the seafloor, and any persisting chemicals diffused or digested by microbes. A robot tasked with charting a plume must be able to forecast where and when it will intersect with different parts of the plume in order to collect useful observations of its spatiotemporal structure, but the state is uncertain as a result of unseen advective forces (e.g., deep currents, topographic updrafts), diffusive mixing, and unknown venting characteristics that dictate plume formation. Point *in situ* measurements in a continuous three-dimensional volume over time make the problem worse, as no single measurement is sufficient to locate the plume.

In addition to the technical challenges of determining a sensing strategy in the face of highly uncertain and dynamic phenomena, robot operational constraints also create planning challenges. In the expeditionary sciences, and particularly within deep-sea research, mobile robots equipped with multi-sensor payloads are increasingly used to perform surveys in these dynamic environments, typically executing preset trajectories hand-designed by human scientists (e.g., [1]). In this mode, the robot cannot react to measurements while executing the set trajectory. Although in dynamic environments such open-loop trajectories can result in sparse measurements of the target phenomenon (plume) or can miss short-lived events entirely [2], this concept of operations remains the state-of-the-art in practical deployments due to their relative ease to encode, limited computational capacity of the platforms, and predictability of robot actions to outside supervisors. In this article, we consider constraints introduced by a specific robot, autonomous underwater vehicle (AUV) *Sentry*. This AUV, operated by the National Deep Submergence Facility (NDSF) at the Woods Hole Oceanographic Institution (WHOI) [43], by operational policy is only permitted to execute pre-determined regular trajectories like “lawnmower” patterns or spirals, making online adaptation impossible.

Enabling robots like *Sentry* to collect scientific observations of spatiotemporal phenomena while operating without access to adaptive behaviors requires an autonomy system that can place operationally-approved fixed trajectory patterns strategically to maximize desirable intersections with the phenomena. To be able to strategize effectively, a means of learning to forward simulate the dynamics of the target environment

over a long-horizon from a small history of robot deployments is required. This is fundamentally a *sequential decision-making problem*, and is closely related to informative path planning (IPP), in which a robot selects behaviors according to an information-theoretic reward function computed over a probabilistic belief of the environment state. Existing methods in IPP (e.g., [2, 44–47]), the related field of experimental design and optimal sensor placement (e.g., [48, 49]), and general decision-making under uncertainty (e.g., [5, 50–52]) have demonstrated how sequential decision making can be applied to sampling scenarios in which online, adaptive behaviors are possible, the phenomenon of interest is static, and/or there is an opportunity to train the belief model from many trials, multiple sensors, or highly adaptive trajectories. Each of these typical scenarios is violated for the expeditionary science sampling problem—online adaptation is not possible, the phenomenon is dynamic, and there are very few total number of deployments for model training.

We directly address the open challenges of sample-efficient dynamics learning and few-step planning sequences under operational constraints unaddressed by the classical informative path planning frameworks with our novel *deployment-by-deployment* sequential decision-making formulation for expeditionary missions, PHORTEX: **P**Hysically-informed **O**perational **R**obotic **T**rajectories for **E**Xpeditions (Fig. 6.1). In PHORTEX, each deployment of the AUV is considered a single action, and each action is composed of a chain of operationally-approved trajectory patterns (e.g., lawnmowers) parameterized by a small set of characteristics (e.g., orientation, origin, resolution). The chain parameters are jointly optimized over a long-range forecast of the spatiotemporal distribution of interest (e.g., plumes) to maximize expected intersections with a moving plume. These forecasts are provided by our probabilistic model PHUMES: **P**Hysically-informed **U**ncertainty **M**odels for **E**nvironment **S**

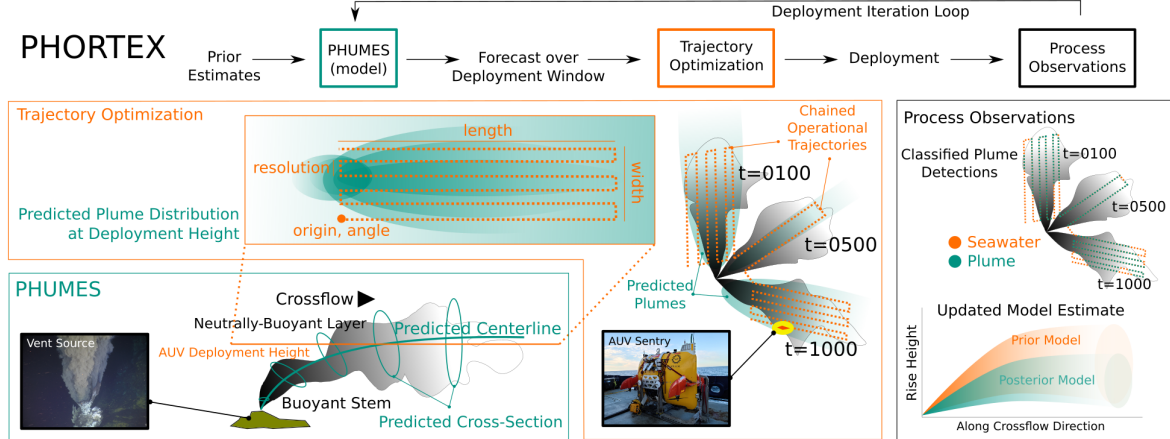


Figure 6.1: An overview of PHORTEX: **P**Hysically-informed **O**perational **R**obotic **T**rajectories for **E**Xpeditions. Over the course of an expedition, an autonomous vehicle is deployed several times. In preparation for a deployment, PHUMES is used to generate a probabilistic forecast of the target spatiotemporal distribution. PHUMES can be seeded with prior information from scientific knowledge, data of opportunity from other deployed sensing equipment, or previous robot deployments. A trajectory optimizer is given the forecasts and modifies the parameters of a trajectory primitive. Several primitives are chained together to form a complete deployment trajectory. The robot is then deployed and executes the trajectory. Following a deployment, *in situ* observations from multiple heterogeneous science sensors are collected from the robot and fused into a data product that can be used to train PHUMES, and the deployment planning process iterates. Here, the task of hydrothermal plume charting with AUV *Sentry* is illustrated. PHUMES generates an forecast of temporally-evolving plume centerlines and cross-sections from estimates of vent characteristics and fluid crossflow (e.g., current) informed by measurements or prior distributions over these variables. For a given height that *Sentry* can operate (and is constrained to operate for any given primitive), chains of uniform coverage lawnmowers are optimized (over parameters such as length, width, resolution, origin, and global angle) with respect to the plume forecast to intersect and track the plume over the course of a deployment window. Following a *Sentry* deployment, observation locations are classified as binary plume detections from analysis of several science sensors. This product is then used to update the PHUMES model of plume centerline and cross-section over time. The new PHUMES model is then used to plan the next deployment of *Sentry*.

6.1.1 CHARTING DEEP-SEA HYDROTHERMALISM

Hydrothermal vents in the ocean were first observed in 1977 at the Galapagos Rift [7], and since have been a concerted focus of geodynamical and biogeochemical studies. Venting sites, energized by magmatic sources, release fluids between 20-400 °C (background deep ocean temperatures are approximately 2 °C) and imbued with minerals,

metals, dissolved gases, and other compounds [53, 54]. These warm, nutrient-pumping sites in the deep ocean have created oases of unique micro- and macro-fauna [7]. Detection and characterization of seafloor hydrothermal venting are critical for understanding fundamental interactions between the deep ocean, its underlying basaltic crust, the deep biosphere, and (bio)geochemical fluxes.

We build on a wealth of work that has primarily focused on localizing hydrothermal venting plume sources (e.g., [39, 42, 55–60]) using a variety of equipment such as ship-based acoustics, towed instrument rosettes, remotely-operated vehicles (ROVs), submersibles, and autonomous underwater vehicles (AUVs). Generally, these methods use detections of anomalous water masses (as determined from *in situ* sensors) to constrain the location of a seafloor vent for specialized seafloor equipment to be subsequently deployed to e.g., estimate bulk chemical or nutrient flux from the vent or characterize the driving magmatic system underneath the crust. The localization methods can be fully offline, in which surveys by vehicles like *Sentry* with no adaptive capacity are post-processed and estimates of vent locations are inferred from a single survey [39, 56], or fully online, in which autonomous gliders with adaptive capabilities utilize gradient descent of similarly myopic adaptive sampling strategies to seek a plume source are used [42]. In [41], an autonomous glider tasked with localizing a vent source could adaptively chain uniform coverage trajectories together with increasingly fine resolution as the robot position converged on an estimate of a plume source location while underway. We emulate this chaining methodology in our trajectory chaining scheme, however the selection of trajectories by PHORTEX is done completely offline before AUV *Sentry* is deployed. Indeed, it is notable that online strategies for hydrothermal plume hunting almost universally employ glider-type robot platforms, which are typically smaller, payload-limited, and less depth-capable than vehicles like *Sentry*. 90% of known vent fields are deeper than 200 m in the ocean, and over 75% are deeper than 1000 m [61]. State-of-the-art gliders are typically not rated deeper than 1000 m, which means that deep-sea research of the majority of vent sites are reliant on vehicles like *Sentry* and demand advances in offline-suited planning techniques.

We also draw on “plume hunting” research in robotics, which has been equivalently styled as odor mapping, odor localization, source localization, and source seeking. In these works, the “source” could be any type of emitting site (e.g., gas, radio, acoustic, odor) and through partial observations of the emitted substance, the source is discovered using techniques that can be divided broadly into biologically-inspired heuristic search (e.g., [62, 63]) or adaptive informative path planning (e.g., [64]). Biological or

heuristic techniques draw (varying-levels of) inspiration from animal or insect behavior in olfactory settings. Such techniques typically include gradient-based algorithms like chemotaxis [65], or algorithms that directly mimic a particular animal [66]. These techniques are typically reactive and myopic, although they have been demonstrated to be relatively robust in open-world settings. In contrast, adaptive informative path planning can be nonmyopic, and typically attempts to embed knowledge (either heuristically or rigorously) about flow-fields (i.e., advection and diffusion) to assist in plume localization. Such techniques also live on a spectrum, from algorithms that resemble biologically-inspired techniques like infotaxis [67] to methods that use model order reduction techniques (like proper orthogonal decomposition) to encode complex numerical models (like the Navier-Stokes equations) into a belief model to better treat complex data [68].

While source discovery remains an important area of research, in this article we focus on how science can be advanced at the hundreds of vents that have been successfully identified. Thus, we pose a complementary problem to source discovery: *given a venting source, what impact do the venting fluids have on the local environment?* In this framing, rather than using detections of a plume as a means of source localization, the detections themselves are the valuable data product for scientific inquiry. By placing instruments throughout an evolving plume structure over multiple length- (meter to kilometer) and time- (hours to days) scales to collect dense in-plume measurements, previously intractable questions with respect to microbial lifecycle and transport, carbon cycling, and anomalous water mass formation, can be approached. Work that has used robots to map or chart plume-like structures has been presented as the “front-tracking” problem [63, 69]. In this problem, two water masses converge (such as the warm hydrothermal fluid and the cold background seawater), and the goal is to use a robotic vehicle to track the edge of these water masses or stay within a single type of water mass. The importance of both multirobot collaboration and online decision-making in these schemes is essential to their efficacy; as far as we are aware, this article is the first to present a water mass tracking solution within an offline optimization strategy with a single agent, and the first to attempt this for the hydrothermal charting problem.

6.1.2 CLOSING THE LOOP: EXPEDITION LOGISTICS FOR DEEP-SEA ROBOTICS

Oceanographic research expeditions are an undertaking that requires the coordination and collaboration of a science party, external engineering teams that maintain and operate the scientific equipment used during studies, and the captain and crew aboard a research vessel (on which everyone lives and works during operations). Deep-sea (depths below the mesopelagic zone starting at 1000 m) capable robotic platforms used in oceanic research are assets independently maintained from a ship, and typically requested on a per-expedition basis. AUV *Sentry* may be deployed on tens of expeditions in a given year, with up to 250 days at sea. Safety of both people and equipment are held to the highest importance. Further, the critical role of *Sentry* in oceanographic research drives the strict operational policies that dictate *Sentry* deployments to prevent vehicle loss or damage.

It is with this context that *Sentry* deployments are designed by the science party and ultimately approved by the *Sentry* engineering team. In a typical workflow, the science party may provide a set of coordinates or waypoints they generate based on bathymetric maps, prior knowledge, or previous data (when available). The *Sentry* team design survey trajectories based on these coordinates and respecting basic operational constraints of the vehicle (e.g., speed, minimum/maximum altitude from the seafloor). With approval of the *Sentry* team, science party, and captain, the survey is then executed. A single “dive” of *Sentry* is multiple hours (typically not less than 5 hours, and under 24 hours). At the conclusion of a dive, *Sentry* is recovered from the ocean and data products containing hundreds of thousands of point measurements from multiple heterogeneous sensors are made available to the science team within a few hours after *Sentry* returns to the deck. Depending on the length of the dive, 12-18 hours of vehicle cycling time (e.g., recharging, instrument maintenance, preparation for the next deployment) are required. Based on the length of a particular expedition and other ongoing research activities, *Sentry* may be deployed only a handful of times.

The complexity of these basic operations for *Sentry* alone, in addition to the burden of coordinating several other ongoing scientific projects happening simultaneously, day-to-day operational changes, and unforeseen discoveries and hurdles make performing “closed loop science” with robot platforms a challenge while at sea. For hydrothermal plume monitoring, a combination of sensor streams need to be used to make confident plume detections [39], but information about exact tidal state, state of the venting

source, and background sea characteristics are typically not available in these products, and can require fusing data products from other instruments deployed on a cruise, if available. The planning challenge is further exacerbated when the design of a new mission requires not just deep analysis of the collected data, but forecasting the implications of those data onto a new day, new site, or new objective.

Our work aims to alleviate the burden of closing the loop onboard a research vessel for AUV operations by positioning PHORTEX as a means of generating interpretable phenomenon forecasts and trajectories through those forecasts that can be informed from diverse data streams, verified by science party members, and approved by *Sentry* engineers. Algorithmically, the formulation of PHORTEX as a sequential decision-making framework produces trajectories which are informed by previous observations, thus literally behaving like a closed-loop controller for robot actions. Through a real field mission to the Gulf of California to chart hydrothermal plumes in the northern Guaymas Basin, we demonstrate how PHORTEX can be practically deployed for plume charting.

6.1.3 CONTRIBUTIONS

In this article, we propose an autonomy system, PHORTEX, which can solve the hydrothermal plume charting problem under operational constraints imposed by a state-of-the-art AUV, *Sentry*. *Sentry*, by policy, can only execute pre-defined trajectories while underway, and can only be deployed a small number of times during a given expedition. As modern IPP, plume-hunting, and front-tracking techniques strongly rely on underway adaptive behaviors, we extend these frameworks for *Sentry* by formulating a *deployment-by-deployment* sequential decision-making problem which treats each pre-defined deployment of *Sentry* as a single action in sequence with few steps. We define each deployment action as a chain of operationally-approved trajectory primitives (i.e., lawnmower patterns), which are parameterized by a small number of characteristics including their relative size, resolution, and position.

To optimize a given chain for tracking a target plume, we introduce a probabilistic model PHUMES, which provides long-horizon forecasts of plume state. As very few deployments of AUV *Sentry* are possible during an expedition, PHUMES must overcome the challenge of sample-efficient dynamics learning from sparse, partial observations. To do so, we leverage the existence of well-characterized analytical models for buoyant plume dynamics used in ocean and atmospheric sciences to embed a numerical simulator into a Bayesian filtering framework. The use of this simulator creates a strong

inductive bias for the dynamics learning problem for a given field site. There are several advantages to this scheme: the forecasts generated by PHUMES are driven by a set of physically-meaningful parameters (e.g., vent temperature, crossflow magnitude) which are interpretable by the science team and over which the science team may have useful prior knowledge; the PHUMES framework can easily accept data or information external to *Sentry* deployments that map to the physically-meaningful parameters; and forecasts that are generated consist of both a mean and variance, providing flexibility for defining reward functions for the trajectory optimization scheme.

We demonstrate PHORTEX and PHUMES in a real field trial for hydrothermal plume charting with AUV *Sentry*. In so doing, we present a method of processing real *in situ* observations taken by instruments on *Sentry* into a data product which can be used to indicate whether a particular observation is plume or ambient seawater. We also discuss the practicalities of using external sensing equipment available during the field trial to benefit the PHUMES formulation. Additionally, through this trial we demonstrate the first iterative offline planning technique for plume charting with deep-sea capable vehicles, illustrating a novel capability for these assets for future research expeditions and putting over 75% of known vent fields in reach for strategic charting and surveying.

Through both the field trial and simulations we demonstrate that *Sentry* using PHORTEX can collect at least as many in-plume observations as the best human-designed trajectories, while improving both spatial and temporal diversity of those samples. The diversity of samples corresponds to observing more unique regions of a plume structure, and has important, positive implications for scientific inquiry to be performed on the dataset collected by *Sentry* in post-expedition analyses.

The rest of this article is organized as follows: in Section 6.2 we formally present the hydrothermal plume charting sequential decision-making problem as a partially-observable Markov decision process (POMDP), in Section 6.3 present PHORTEX, in Section 6.4 and ?? respectively present field results and simulation results, in ?? further discuss specific choices made in the definition of PHORTEX for the hydrothermal plume charting problem and argue how PHORTEX can be generalized for other scientific expedition contexts and tasks, in ?? present additional related work, in ?? highlight other open challenges for robotics in expeditionary science, and in ?? provide closing remarks.

6.2 PROBLEM FORMULATION

During scientific expeditions, the objective of a robot is to collect informative measurements as defined by a task-specific query (e.g., reduce uncertainty over a quantity, find the global optimum in a distribution, track a moving target). In the instance of hydrothermal plume charting, the goal is to map or “chart” the spatiotemporal structure of a buoyant plume using a dynamically constrained AUV. Such a chart enables scientists to infer relevant scientific properties of generating vents (e.g., chemical flux) and to create detailed models of deep-sea interactions and nutrient cycling.

6.2.1 SCIENTIFIC EXPEDITIONS AS A SEQUENTIAL DECISION-MAKING PROBLEM

These missions require a robot to make a sequence of decisions to collect scientifically useful measurements of an unknown, partially-observable spatiotemporal environment under operational constraints. We formulate this sequential decision-making problem as a partially observable Markov decision-process (POMDP). Let $\Pi(\cdot)$ denote the space of probability distributions over the argument. A finite horizon POMDP can be represented as tuple: $(\mathcal{S}, \mathcal{A}, T, R, \mathcal{Z}, O, b_0, H, \gamma)$, where \mathcal{S} are the states, \mathcal{A} are the actions, and \mathcal{Z} are the observations. At planning iteration t , the agent selects an action $a \in \mathcal{A}$ and the transition function $T : \mathcal{S} \times \mathcal{A} \rightarrow \Pi(\mathcal{S})$ defines the probability of transitioning between states in the world, given the current state s and control action a . The transition function governs both how the state of the robot will evolve, given a chosen action, and the potentially stochastic evolution of the underlying spatiotemporal environment, such as the plume centerline. After the state transition, the agent receives an observation according to the observation function $O : \mathcal{S} \times \mathcal{A} \rightarrow \Pi(\mathcal{Z})$, which defines the probability of receiving an observation, given the current state s and previous control action a . The reward function $R : \mathcal{S} \times \mathcal{A} \rightarrow \mathbb{R}$ serves as a specification of the task, assigning the states of the world that are useful for a given scientific objective high reward and others low reward. A POMDP is initialized with belief $b_0 \in \Pi(\mathcal{S})$ — an initial probability distribution over state — and plans over horizon $H \in \mathbb{Z}^+$ with discount factor $\gamma \in [0, 1]$.

As the robot moves through the world, it selects actions and receives observations. Since the state of the world is not directly observable in a POMDP, the robot maintains a probability distribution over possible states (i.e., belief) and must update this distri-

bution each time it takes an action and receives an observation. Given the transition and observation models, the belief can be updated directly using a Bayes filter [3]:

$$\tau(b_{t-1}, a_{t-1}, z_t) = b_t \triangleq \Pi(S_t | a_0, z_0, \dots, a_{t-1}, z_{t-1}, z_t) \quad (6.1)$$

$$= \Pi(S_t | b_{t-1}, a_{t-1}, z_t) \quad (6.2)$$

$$= \frac{\int_{s \in \mathcal{S}} O(s, a_{t-1}, z_t) T(s, a_{t-1}, s') b_{t-1}(s')}{\Pi(z_t | b_{t-1}, a_{t-1})} \quad (6.3)$$

where $\tau(b, a, z)$ is the updated belief after taking control action a and receiving observation z (Eq. 6.3). Unfortunately, Eq. (6.3) is intractable to compute directly and an approximate Bayesian inference procedure is required to represent the belief (e.g., a Kalman filter [4], a particle filter [5], or variational methods [70, 71]).

Due to the stochastic, partially observable nature of current and future states, the realized reward in a POMDP is a random variable. Optimal planning is defined as finding a horizon-dependent policy $\{\pi_t^* : \Pi(\mathcal{S}) \rightarrow \mathcal{A}\}_{t=0}^{H-1}$ that maximizes expected reward: $\mathbb{E}\left[\sum_{t=0}^{H-1} \gamma^t R(S_t, \pi_t(b_t)) | b_0\right]$, where b_t is the updated belief at time t , conditioned on the history of actions and observations. The recursively defined horizon- h optimal value function V_h^* quantifies, for any belief b , the expected cumulative reward of following an optimal policy over the remaining planning iterations: $V_0^*(b) = \max_{a \in \mathcal{A}} \mathbb{E}_{s \sim b}[R(s, a)]$ and

$$V_h^*(b) = \max_{a \in \mathcal{A}} \mathbb{E}_{s \sim b}[R(s, a)] + \gamma \int_{z \in \mathcal{Z}} \Pi(z | b, a) V_{h-1}^*(\tau(b, a, z)) dz \quad h \in [1, H - 1], \quad (6.4)$$

The optimal policy at horizon h is to act greedily according to a one-step look ahead of the horizon- h value function. However, Eq. (6.4) is intractable for large or continuous state, action, or observation spaces and thus the optimal policy must be approximated. Much of the art of practical decision-making uncertainty is making well-designed algorithmic and heuristic choices that enable efficient and robust planning algorithms.

6.2.2 SEQUENTIAL DECISION-MAKING WITH AUV *Sentry*

AUV *Sentry* is capable of autonomously navigating between given waypoints using a closed-loop controller and a state estimator that uses acoustic ranging between the robot and the ship to set latitude, longitude, and depth coordinates. At present, *Sentry* is not capable of *underway* decision-making in which waypoints are adaptively set on-

the-fly while the robot is executing its mission. The lack of underway abilities is both a logistical and policy obstacle. Logistically, computational resources available in the robot itself are not capable of computing actions that address the POMDP. Due to the reliance of acoustic communication between the robot and ship, data from *Sentry* cannot be streamed to an external computing resource densely enough to be informative (science data communication between ship and robot is 0.02 Hz assuming no packet loss, and only a subset of sensor data can be made available in any given packet). By policy, *Sentry* trajectories are rigorously vetted before each dive using bathymetric maps of the target region and dynamics validation schemes. Extreme (and warranted) risk aversion to losing or damaging *Sentry* leads to the policy that underway plan changes cannot be part of normal operating procedures.

Thus, to enable sequential decision-making with *Sentry* requires consideration of *deployment-by-deployment* autonomy. Unlike underway decision-making, deployment-by-deployment autonomy does not modify the AUV trajectory in real-time, but instead leverages the “down-time” between robot deployments to post-process data, update a belief model about the environment, and plan a new fixed trajectory for the next deployment to execute. This form of autonomy honors the strong requirement that each deployment must pass through a rigorous safety and validation check, while enabling adaptive search behavior based on accrued knowledge. Each planning “step” or iteration in the POMDP framework is an entire deployment of *Sentry*. In the following section, the implications of this constraint are codified within a POMDP framework.

6.2.3 CHARTING HYDROTHERMALISM AS A POMDP

THE STATE SPACE \mathcal{S} The state space of the plume-charting POMDP consists of the joint continuous states of the environment (i.e., the plume) and the robot. The environment state will be represented by a d -dimensional vector of continuous plume parameters $\mathbf{x}_p \in \mathbb{R}^d$ and a current vector $\mathbf{x}_c \in \mathbb{R}^2$ that contains the heading and velocity of the prevailing crossflow, which vary in time and drive the movement of the plume. The robot state will be represented by a vector $\mathbf{x}_r \in \mathbb{R}^3$ that represents the latitude, longitude, and depth of the robot.

THE ACTION SPACE \mathcal{A} The action space of the plume-charting POMDP consists of sequences of parameterized lawnmower (i.e., back-and-forth uniform coverage) pattern trajectory primitives. The selection of the “lawnmower” as the base primitive was given by *Sentry* operators. By chaining lawnmower trajectories together during a deployment,

a relatively expressive action set is available. Each trajectory primitive is parameterized by a set of real-valued parameters $\theta \in \Theta \subseteq \mathbb{R}^b$. These parameters include scale (length and width that describe the rectangle in which the lawnmower is contained), resolution (the absolute distance between tracklines of the lawnmower), and global position (latitude-longitude-depth coordinate and planar angle of the origin of the primitive). The robot’s action set then consists of sequences of parameterized trajectories, i.e., $\mathcal{A} = \Theta^n$, $n \in \mathbb{Z}^+$. The number of trajectory objects n and the altitude or depth for which a trajectory will be executed for a given chain is fixed *a priori* to planning.

THE TRANSITION FUNCTION T The transition function $T(s, a, s')$ will be decomposed into a plume transition T_p , a current transition T_c , and a robot transition function T_r .

- The plume state parameters \mathbf{x}_p , e.g., venting characteristics like plume exit velocity or vent temperature, are assumed to be constant and therefore the plume transition function T_p is given by: $T_p(\mathbf{x}_p, a, \mathbf{x}'_p) = \delta_{\mathbf{x}_p=\mathbf{x}'_p} \forall a \in \mathcal{A}, \mathbf{x}_p, \mathbf{x}'_p \in \mathbb{R}^d$. Although it is possible for plume parameters to vary on a timescale relevant to a robotic deployment (over the course of hours [72]), the overall impact to gross features of plume rise height, bend angle, and cross-sectional area is essentially negligible, which is reflected in the form of the transition function provided.
- The current transition function T_c is more complex and driven by tidal cycles, local bathymetry, and deep sea currents. We will learn the current transition function $T_c(\mathbf{x}_c, a, \mathbf{x}'_c) = \delta_{\mathbf{x}'_c=h(\mathbf{x}_c)} \forall a \in \mathcal{A}, \mathbf{x}_c, \mathbf{x}'_c \in \mathbb{R}^2$, where the function h evaluates the future current magnitude and heading from the present current state, from point observations of current magnitude and heading from a sensor that is not part of the robot (described in detail in Section 6.3.2). The use of a separate sensing system makes learning this transition function independent of robot actions. However, if a similar sensor were available on the robot, this learned transition function would be dependent on robot actions.
- The robot transition function T_r assumes that the robot’s waypoint controller is deterministically able to execute a planned trajectory: $T_r(\mathbf{x}_r, a, \mathbf{x}'_r) = \delta_{\mathbf{x}'_r=g(\mathbf{x}_r, a)}$, where the function g evaluates the goal waypoint of the trajectory given by a . Although there is some uncertainty in the robots transition, in practice in our field application, localization and control were well-solved problems and pose uncertainty contributed minimally to the robot’s task execution compared with uncertainty about the plume state.

THE REWARD FUNCTION R The reward function for the plume-charting POMDP encodes the robot’s objective to produce a comprehensive map of the plume. We choose to approximate this objective by rewarding the robot for collecting observations of “plume fluids”, i.e., water that is expected to be derived from hydrothermal vents as indicated by our belief of the environmental state $R([\mathbf{x}_p, \mathbf{x}_c, \mathbf{x}_r]^\top, a) = \mathbb{I}[\text{in_plume}(\mathbf{x}_p, \mathbf{x}_c, \mathbf{x}_r, a)]$.

THE OBSERVATION SPACE \mathcal{Z} The robot carries a variety of scientific sensors. We use a sensor model that fuses and converts these complex, continuous scientific observations into a simplified measurement of plume content in a given fluid parcel $z_p \in \{0, 1\}$, discussed in Section 6.3.1. By performing this filtering step, we significantly reduce the dimensionality and complexity of the observation space. Outside of the robot, a sensing system provides independent observations of current magnitude $z_g \in \mathbb{R}^+$ and heading $z_h \in \{(-180, 180]\}$. Thus $\mathcal{Z} = [z_p^n, (z_g, z_h)^m] n, m \in \mathbb{Z}^+$.

THE MEASUREMENT FUNCTION O The measurement function encodes the relationship between the plume parameters and heterogeneous scientific sensors on the robot, the prevailing current with the external sensing system deployed by the science party, and the robot location with the navigation equipment aboard the vehicle and ship. We make use of a sensor model described in Section 6.3.1 to process scientific sensor data into a measurement that indicates whether a fluid parcel was derived by a plume, and utilize PHUMES (Section 6.3.3) to map both current data and the simplified plume measurement to plume parameters. We assume that the robot position is fully-observable and exactly reported by the navigation equipment.

THE HORIZON H AND DISCOUNT FACTOR γ In deployment-by-deployment autonomy, the horizon H can be set to be equal to the total number of deployments to be conducted during an expedition and the discount factor γ set to 1.0. However, practically the state of *Sentry* at the end of one deployment has little or no impact on its achievable reward in the subsequent deployment due to the delayed nature of deployments and the requirement that *Sentry* always start and end on a stationary ship. This has the impact of setting $\gamma = 0$ and breaks the finite-horizon sequential decision making problem into a sequence of horizon-1 planning problems. This reduces the capacity of the planner to reason about long-term, multi-dive information gathering actions, but computationally simplifies the planning problem.

6.3 METHODOLOGY

To solve the plume-charting POMDP as described in Section 6.2.3, we present a specific instance of PHORTEX, which first utilizes a physically-informed probabilistic model (PHUMES) to generate forecasts of spatiotemporal distributions of plume fluids and then optimizes chains of trajectory primitives (e.g., lawnmowers) to maximize the total number of observations of those plume fluids. PHORTEX iteratively improves the performance of these trajectory chains for each deployment of AUV *Sentry* using the history of collected observations from the robot’s heterogeneous science sensors.

6.3.1 PLUME DETECTION: TREATMENT OF ROBOTIC SCIENCE SENSORS

For any instance of PHORTEX, it will be necessary to process continuous measurements from multiple science sensors into a product that can be used to train the PHUMES model. For some combination of sensors and tasks, there may be a sensor for which the continuous signal can be directly used—for instance, using optical backscatter for finding the most densely populated algal patch—but in the hydrothermal charting task, there is no one sensor that can be used directly as a proxy for whether a parcel of fluid was hydrothermally derived [39]. This lack of exact sensing is due to the variable rates for which temperature, chemistry, and particulate matter persist within a plume structure. While temperature anomaly is a strong indicator for a buoyant stem, in the neutrally-buoyant layer temperature anomaly may be on the scale of noise of the sensor (only a few hundredths of a degree). Chemistry anomaly can persist longer within a plume, but is subject to unknown and variable rates of microbial digestion, and some chemical signatures can be tied to other oceanographic processes (such as mixing of stratified layers in the water column) that may be a false signal. Elevated particulate density can be a strong signal in the neutrally-buoyant layer for hydrothermalism derived from “smoking” vents, but not every vent will produce plumes with dense particulates. Taken together, this environmental complexity requires developing a sensing strategy that can fuse observations from multiple science sensors onboard AUV *Sentry* into a data product which can helpfully indicate whether the robot encountered plume fluids.

We elect to create a binary measurement, drawing on the work in [39], to indicate whether *Sentry* was in a plume or in background seawater. The following sensors are used to compute this measurement: conductivity probe (salinity), temperature probe

(temperature), oxidation-reduction potential (ORP) instrument (relative “reactivity” of water), optical backscatter (OBS) instrument (turbidity), optode (oxygen), and experimental spectroscopic instruments Pythia and SAGE (dissolved methane). Sensors are internally logged at variable rates, but sub-sampled to a fixed 1 Hz sampling rate with a shared clock time for the purposes of directly comparing the instruments. Each of these sensors has its own physical characteristics and response to the chemistry of plume water. For example, ORP exhibits a large negative spike when first encountering plume water and then a slow hysteresis back to a nominal values. Measurements of salinity, temperature, and oxygen are expected to be influenced not only by plume water, but background physical mixing in the ocean; in contrast, turbidity, ORP, and methane are signals strongly associated with hydrothermalism because they are not persistent in typical seawater. To account for the different ways in which sensors respond to plume waters, an individualized processing regime is used for each sensor to detect “potential plume masses” in each stream (see Table 6.1), then weights are assigned to each sensor based on their individual reliability with respect to identifying plume water, as assigned by the science party and consulted experts in preparation for the research expedition. A corroboration scheme is then used to classify observations, in which the weighted detections for each sensor are summed together and a threshold set to identify an observation as “plume” or “background”. A total corroboration score of 4 or more was used to classify an observation as “plume”. An example of this sensor applied to real *Sentry* detections is shown in Fig. 6.2.

Quantity	Positive Plume Detection Criteria
Salinity	Detrended practical salinity outside 3 standard deviations of the entire time series
Temperature	Detrended temperatures above the 75th percentile of entire time series
ORP	Detections less than -0.005
OBS	Optical attenuation above the 75th percentile of entire time series
Oxygen	Detrended concentrations outside one-hour rolling computation of 3 standard deviations
Methane	Normalized concentration above 0.3

Table 6.1: Instruments on AUV *Sentry* and the criteria used to identify plume fluids for each instrument. The weight is used to indicate relative “trustworthiness” of a plume detection for each sensor, and is used in a corroboration scheme that sums detections across sensors in order to make a final determination on whether an observation location contained a parcel of plume fluid or consisted of background seawater. “Detrending” data removes depth-related cross-sensitivity from the measurements; for example, temperature is stratified in the deep ocean, so to ignore the impacts of depth changes in the data stream, those effects are removed by “detrending” the data stream.

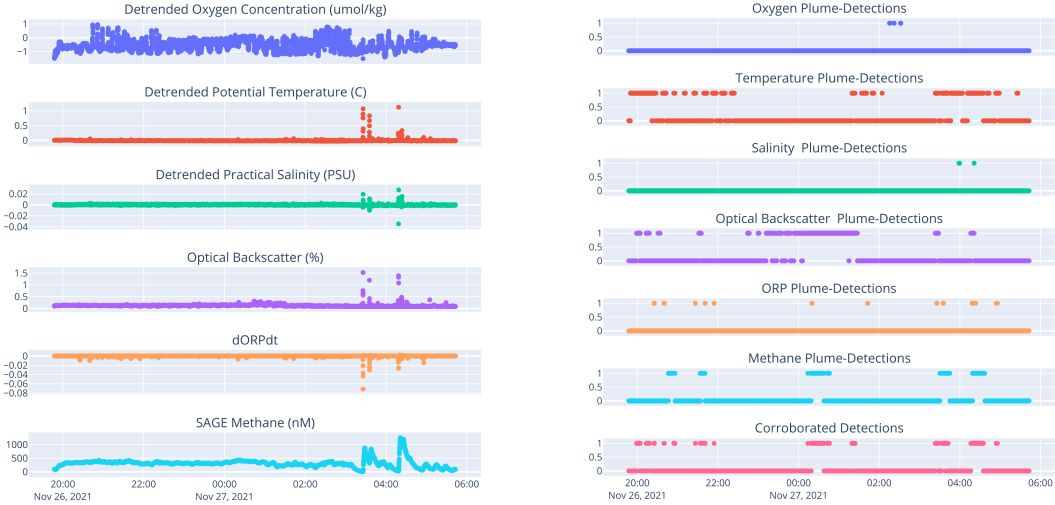


Figure 6.2: Example time series (left) and associated detections (right) over the AUV *Sentry* sensor suite. Oxygen, temperature, and salinity measurements are detrended using a linear transformation fit to depth vs. value plots. The time series demonstrates two types of plume detections. The first are “obvious detections” in which most sensors register strong anomalies (this happened twice toward the end of the deployment) and are most strongly associated with buoyant-stem derived fluids. The second are “persistent-plume detections” in which the robot traverses through water that is slightly more turbid, warm, or chemical-rich than background water over potentially long horizons (this happened early in the deployment and in the middle). Such detections are most strongly associated with neutrally-buoyant layers. The conservative corroboration detector successfully identifies both forms of plume water.

The result of our sensor model is to convert multiple, time-stamped sensor observations $s_{t,i} \in \mathbb{R}$, $i = 1, \dots, S$ to a single, binary plume-detection $z_p \in \{0, 1\}$. These binary plume detections are then used to update our plume model and plan robot trajectories, as described in the following sections. The accuracy of this sensor model is currently uncharacterized, as there is no available ground truth in a field setting by which to verify the assigned classifications. Qualitatively, the classifications were reviewed by the science team and verified for their alignment with expert opinions on which label to assign.

6.3.2 EXTERNAL SENSING: LEVERAGING ALL AVAILABLE INFORMATION

Outside of AUV *Sentry*, several sensing packages were deployed during the research cruise which collect relevant information about the state of temporally evolving cross-flow and ambient seawater properties. We leverage these external measurements within our PHUMES instance in two ways: (1) setting default seawater constants of the target site, and (2) to learn the crossflow transition function T_c .

On the first point, measurements from a temperature and salinity sensor mounted to a ship-board rosette were used to define the density, temperature, and salinity stratification curve of the Guaymas Basin water column. The stratification curve is a function that describes the changes in density (or temperature and salinity) over depth in the ocean, and has implications for how a hydrothermal plume will interact with background seawater. The stratification function is used within the physically-informed layer of PHUMES and treated as a constant throughout the expedition. This information could be equivalently extracted from sensors onboard *Sentry*, but the available external sensing package was higher fidelity for the purpose of water column characterization. Moreover, as this information can be observed once and assumed to be effectively constant, it is convenient to incorporate this information outside of the sequential decision-making process.

On the second point, critically there was no “current sensor” on *Sentry* available during our expedition that could be used to measure the *in situ* current magnitude and heading during a deployment. While it may be possible to estimate T_c solely from the binary observations of the plume, access to an external bottom-mounted tiltmeter on the seafloor during this expedition significantly relieved the burden of this inference process. We learn T_c (or, more precisely, the function h by which T_c is defined) by fitting a Gaussian process (GP) with composite radial-basis-function and periodic kernel functions to point observations of crossflow magnitude and heading observed by the tiltmeter. Approximately 3 days of observations were available for training. Crossflow parameters \mathbf{x}_c in \mathcal{S} were set with the expected mean of the trained GP. Presently, a crossflow sensor is in development for *Sentry* using existing acoustic technology onboard the robot; in such a configuration, the process of estimating T_c would be dependent on robot actions and would be a less independent process to the plume-charting task.

6.3.3 PHUMES: PHYSICALLY-INFORMED PROBABILISTIC FORECASTS

PHUMES is a model class that can generate predictions of the distribution of a spatiotemporally evolving state from a history of sparse state-space observations. To quickly learn a predictive model of a spatiotemporal phenomenon, PHUMES leverages access to analytical scientific simulators (when available) codified as systems of ordinary differential equations (ODEs). These simulators reduce the dimensionality of the inference problem from the full-state of the environmental phenomenon (e.g., a 4D volume in space and time with continuous phenomenon measurement) to the dimensionality of the initial conditions and parameters of the simulator (which can then be used to populate the full-state for planning purposes). The use of ODE systems, as opposed to high-fidelity numerical simulators using partial differential equations (PDEs) is intentional; the computational requirement of most PDE systems used to model environmental phenomenon at the scales studied during expeditionary missions are intractable. In contrast, ODE systems are less well-resolved, but summarize the structure of an evolving phenomenon in a useful way that can be enhanced by a generic probabilistic formulation wrapping the ODEs.

In the PHUMES formulation for hydrothermal plume charting, we use a time-averaged model of plume evolution through a weakly stratified fluid under crossflow as described in [35] which we notate as function $f(\cdot, \cdot)$. The crossflow “bends” the buoyant stem of the plume, and reduces the effective rise height of the plume by introducing more mixing. Using a modified cylindrical coordinate system in which s represents a point along the axis described by the plume centerline and θ describes the vertical angle from the base of the plume, our PHUMES simulator takes the form:

$$\frac{dQ}{ds} = Q \sqrt{\frac{2(1 + \lambda^2)}{M\lambda}} (\alpha |\frac{M}{Q}| - U_a \cos \theta| + \beta |U_a \sin \theta|) \quad (6.5)$$

$$\frac{dM}{ds} - U_a \cos \theta \frac{dQ}{ds} = \frac{FQ}{M} \sin \theta \quad (6.6)$$

$$U \sin \theta \frac{dQ}{ds} + M \frac{d\theta}{ds} = \frac{FQ}{M} \cos \theta \quad (6.7)$$

$$\frac{dF}{ds} = -QN^2 \sin \theta \quad (6.8)$$

$$x_a = \int_0^s \cos \theta ds \quad (6.9)$$

$$h_a = \int_0^s \sin \theta ds \quad (6.10)$$

where $U_a = U_a(z)$ is the ambient crossflow velocity, $Q = Q(s, \theta)$ represents the plume specific volume flux, $M = M(s, \theta)$ is the specific momentum flux, $F = F(s, \theta)$ is specific buoyancy flux, N is the Brunt-Väisälä frequency, λ is the ratio of the minor and major axis that define the plume cross-sectional ellipse, x_a and h_a represents the Cartesian transform of s and θ within the plume's frame of reference, and α and β are vertical and horizontal entrainment coefficients. To convert abstract notions of buoyancy and momentum flux to directly observable/meaningful vent characteristics like vent area or fluid exit velocity, we can use the following relationships:

$$Q_0 = \lambda u_0 \frac{A_0}{\pi} \quad (6.11)$$

$$M_0 = Q_0 u_0 \quad (6.12)$$

$$F_0 = g 10^{-4} (T - T_0) Q_0 \quad (6.13)$$

where A_0 is the vent area, u_0 is the initial fluid velocity leaving the vent, T is the temperature of fluid at the vent, and T_0 is the temperature of ambient seawater at the depth of the vent (note that temperature is the dominant component of density, ρ , for deep-sea hydrothermal plumes). Indeed, temperature, area, and exit velocity compose a sufficient set of parameters for representing the initial conditions of any particular plume and plume envelope calculation; these quantities, in addition to the mixing coefficients, form our set of \mathbf{x}_p in \mathcal{S} in the plume-charting POMDP. U_a and the global heading of the crossflow, Θ_a (not directly modeled in these equations, but can be trivially applied to x_a and x_h to convert plume-reference coordinates to global coordinates), form the parameters in \mathbf{x}_c in \mathcal{S} .

With the simulator defined, we can now pose a specific inference problem: from observations of plume or background waters, what are the generating initial conditions (vent area, vent fluid temperature, vent fluid exit velocity) and seawater properties (horizontal mixing coefficient, vertical mixing coefficient, global current heading (at a moment in time), and global current magnitude (at a moment in time))? This explicitly allows us to place probability distributions over \mathbf{x}_p and \mathbf{x}_c , over which we initially place an uninformative prior, $\Pi(\mathbf{x}_p)$ and $\Pi(\mathbf{x}_c)$ and aim to learn the posterior distributions $\Pi(\mathbf{x}_p|\mathcal{Z})$ and $\Pi(\mathbf{x}_c|\mathcal{Z})$ ¹.

¹We effectively separate inference over \mathbf{x}_p and \mathbf{x}_c given the observation model available; indeed we assume that observations of crossflow can be treated as independent of observations of plume detections. This is strongly supported in the practical deployment of *Sentry*, when an external sensor was necessary to observe crossflow. If instead the sensors were co-located on *Sentry*, inference over the joint posterior $\Pi(\mathbf{x}_p, \mathbf{x}_c|\mathcal{Z})$ could be done instead.

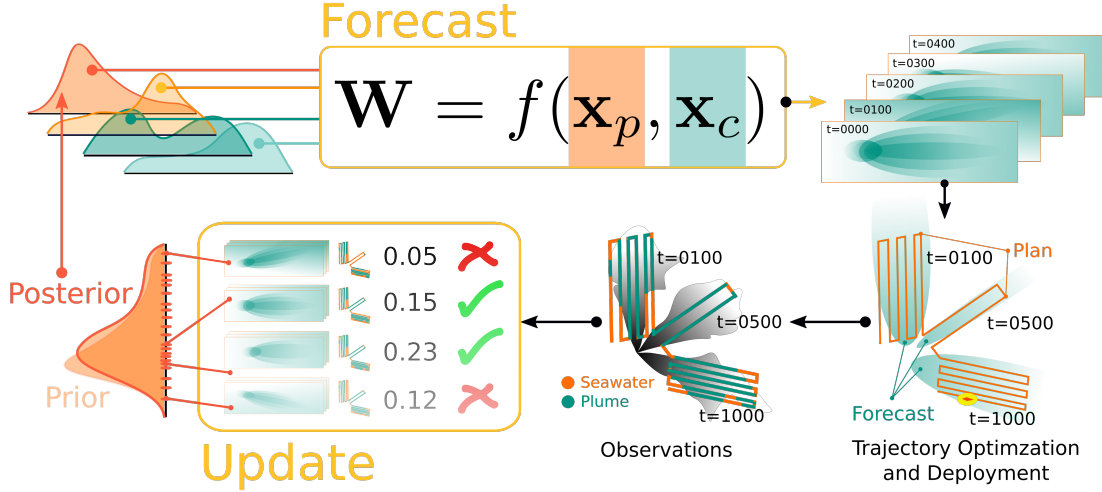


Figure 6.3: PHUMES: **P**Hysically-informed **U**ncertainty **M**odels for **E**nvironment **Sf(\cdot, \cdot) that approximates the physics-driven evolution of a target distribution. This model is seeded with many samples from distributions placed over initial conditions, physical parameters, or temporal functions (such as \mathbf{x}_p and \mathbf{x}_c here). The composite result of this process is a forecast \mathbf{W} that consists of a mean and variance of phenomenon occupancy in a 3D volume over snapshots of time. This forecast is provided to a trajectory optimizer which sets a deployment trajectory that is executed by a robot. The deployment generates a series of observations, which are then used to update the distributions of the generating distributions via an MCMC procedure which compares the gathered observations with the simulated observations of samples from the generating distributions. The resulting posterior update over the generating distributions is then used for the next planning iteration.**

PHUMES consists of two key phases: forecasting (forward simulation) and updating (inverse problem) (Fig. 6.3). In the forecasting step, samples from the distributions of the initial conditions and seawater properties seed the simulator which is solved many times to create a set of plume-envelope samples in the full state space of the target phenomenon (and trajectory optimizer). Time is discretized over domain-specific key points, and any parameters reliant on time are sampled at those discrete points. The set of composite samples at each time is a “forecast” that is essentially a series of “snapshots” of the phenomenon. Precisely, PHUMES generates a time-indexed $t \in \mathbb{T}$ composite estimate of the distribution of plume fluid in a 3D volume $\bar{\mathbf{W}}$ by forward simulating time-dependent M samples of the states $x_{p,t}^{(m)} \sim \Pi(\mathbf{x}_p(t))$ and $x_{c,t}^{(m)} \sim \Pi(\mathbf{x}_c(t))$ through the plume simulator $f(\cdot, \cdot)$:

$$\bar{\mathbf{W}}_t = \frac{1}{M} \sum_{m=1}^M f(x_{p,t}^{(m)}, x_{c,t}^{(m)}) \quad \forall t \in \mathbb{T}. \quad (6.14)$$

The complete forecast $\bar{\mathbf{W}}$ is then used by a trajectory optimizer to approximate the reward function $R([\mathbf{x}_p, \mathbf{x}_c, \mathbf{x}_r]^T, a) = \mathbb{I}[\text{in_plume}(\mathbf{x}_p, \mathbf{x}_c, \mathbf{x}_r, a)] \approx \mathbb{I}[\text{in_plume}(\bar{\mathbf{W}}, a)]$. Equivalently, \mathbf{W} is the robot's belief b . The variance of the forecast \mathbf{S}_W^2 can be similarly computed, depending on the requirements of the reward function.

After the trajectory optimizer yields a plan, *Sentry* is deployed. For a single deployment, upwards of 20,000 observations may be available (each deployment is a minimum of 6 hrs in duration, up to 24 hrs, and sensor measurements are logged at 1 Hz). Using the filter described in Section 6.3.1, AUV *Sentry* provides observations of binary plume detections. Other sensors of opportunity described in Section 6.3.2 provide continuous crossflow magnitude and heading observations. These observations are collated into the sensor model \mathcal{Z} .

At the update step of PHUMES, the distributions over \mathbf{x}_p and \mathbf{x}_c are updated from observations \mathcal{Z} . To find $\Pi(\mathbf{x}_c|\mathcal{Z})$ we use GP models for crossflow magnitude and heading as described in Section 6.3.2. A bulk, closed-form analytic update is made to the GP kernel parameters following typical procedures [73]. For $\Pi(\mathbf{x}_p|\mathcal{Z})$, we use a random-walk Metropolis-Hastings MCMC method [74] to perform the update. Simulations of deployments are generated by solutions to the numerical model seeded with samples from \mathbf{x}_p and \mathbf{x}_c . The output of the simulations is directly compared via a likelihood model with the observations binary observations of plume waters collected by *Sentry*. In practice, the likelihood model uses a false positive rate (the observation is a 1, and the simulation is a 0) and false negative rate (the observation is a 0, and the simulation is a 1) established in consultation with instrument experts on the science team; they are set to 0.1 and 0.3, respectively. With the likelihood model applied, samples of \mathbf{x}_p are then stochastically accepted or rejected. As this inference method is a chaining procedure, the samples of \mathbf{x}_p selected in this procedure are informed by the last, and the cumulative distribution of accepted samples is guaranteed to converge to the true underlying distribution for each of the elements in \mathbf{x}_p . The posterior distribution $\Pi(\mathbf{x}_p|\mathcal{Z})$ is set as the new sampling distribution for the next forecast to be generated.

6.3.4 TRAJECTORY OPTIMIZATION FOR PATH PLANNING WITH FIXED PRIMITIVES

[TODO: some edits are necessary to this section based on feedback; particularly separating the definition of the optimization from the implementation details]

To solve the plume-charting sequential decision-making problem, we begin with the POMDP value function Eq. (6.4) and introduce the model defined in Section 6.2:

$$V_h^*(b) = \max_{\{\theta_1, \dots, \theta_n, n | \theta_i \in \Theta, n \in \mathbb{Z}^+\}} \mathbb{E}_{[\mathbf{x}_p, \mathbf{x}_c, \mathbf{x}_r]^\top \sim b} [R([\mathbf{x}_p, \mathbf{x}_c, \mathbf{x}_r]^\top, \{\theta_1, \dots, \theta_n\})] \quad h \in [0, H-1], \quad (6.15)$$

where $\theta \in \Theta$ parameterizes individual trajectory primitives in a length- n sequence of chained trajectories and b is the planner's belief about the state of the plume, currents, and robot, and the discount factor γ has been set to zero to encode our single-dive planning approximation. Solving Eq. (6.15) still involves the challenging optimization of n trajectories and the joint optimization of all n trajectories into a chain. To simplify the planning problem, given the constraints of real-world robotic deployments, we assume that the number of chained trajectories is given, i.e., $n = N$, and that each trajectory can be optimized independently. This results in the following approximation:

$$V_h^*(b) \approx \max_{\theta_1 \in \Theta} \dots \max_{\theta_N \in \Theta} \mathbb{E}_{[\mathbf{x}_p, \mathbf{x}_c, \mathbf{x}_r]^\top \sim b} [R([\mathbf{x}_p, \mathbf{x}_c, \mathbf{x}_r]^\top, \{\theta_1, \dots, \theta_N\})] \quad h \in [0, H-1]. \quad (6.16)$$

We solve Eq. (6.16), which defines multiple, independent, non-convex, constrained optimization problems, using the trust-constrained method in the `scipy` optimization library for a fixed number of iterations [75]. To evaluate the reward function $R([\mathbf{x}_p, \mathbf{x}_c, \mathbf{x}_r]^\top, \{\theta_1, \dots, \theta_N\})$, we define a trajectory sampler operator $\mathcal{G} : \Theta \rightarrow \mathbb{R}^{3 \times k}$ that takes a trajectory parameter vector as input and produces a set of locations in \mathbb{R}^3 that will be sampled when the robot executes the trajectory, where k is the number of sampled points. These sample points can then be compared with the plume forecast \mathbf{W} produced by PHUMES to count the number of sample points that are contained within the inferred plume.

In practice, we choose our trajectory class to be a lawnmower trajectory, which were parameterized by a vector θ that determines the origin, orientation, height, width, and resolution of the lawnmower. The trajectory sampler \mathcal{G} produces the lawnmower

specified by θ and then subsamples uniformly along its length. We defined the set Θ to enforce that the lawnmower trajectories are contained within a pre-defined, rectangular safe region and that each lawnmower obeys a time-based budget constraint.

6.3.5 AT SEA OPERATIONS

When performing field operations on the research vessel with AUV *Sentry*, we used PHORTEX to enable deployment-by-deployment autonomy that could iteratively improve robot performance with each deployment (Fig. 6.4). Functionally, the trajectories planned with PHORTEX were provided to the *Sentry* engineering team for extensive safety validation prior to each deployment. If approved by the *Sentry* team, the chief scientist, and captain of the vessel, the trajectories were downloaded into the *Sentry* mission planning software as static waypoints. This confirmation process required a lead time of approximately 6 hrs before a given deployment time, and approximately 12 hrs were available between deployments to mechanically service *Sentry* and recharge batteries. The ability of PHORTEX to produce viable trajectories from data within the first 6 hrs that *Sentry* was on-deck following a recovery was critical for keeping this strict timeline. Given the long lead time between trajectory design and *Sentry* deployment, there were many opportunities for the time of a deployment to change due to developments in weather, other science/technology priorities, a critical personnel was occupied, etc. To be robust to these changes, we provided deployment plans that started several hours before and several hours after a given deployment time, and the *Sentry* team truncated the plan at the appropriate point once a deployment time was known with certainty.

6.4 FIELD DEPLOYMENT: CHARTING DEEP-SEA HYDROTHERMAL PLUMES

In November 2021, a research cruise aboard the Research Vessel (R/V) *Roger Revelle* was conducted to the Northern Guaymas Basin in the Gulf of California to study a recently discovered hydrothermal ridge [26, 27]. The research cruise had several objectives: test novel *in situ* instruments to measure dissolved methane, test novel *in situ* instruments to measure the carbonate cycle, map the heat distribution in shallow sediments above hydrothermal sills, collect specimens of tubeworms, and collect biological samples of microbiota in hydrothermal plume-fluids for *ex situ* analysis to re-construct

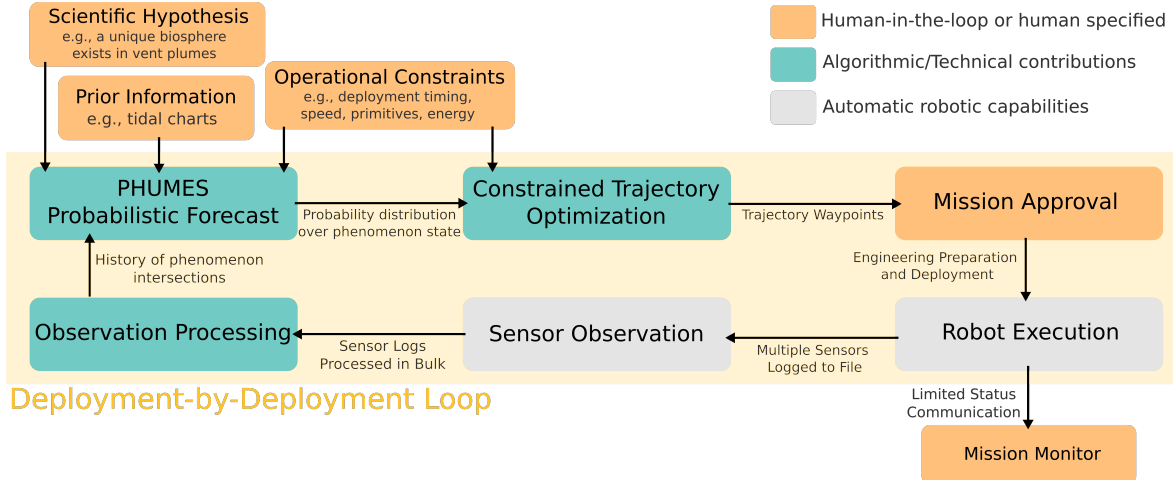


Figure 6.4: The at-sea operations implementation of PHORTEX. Integration of scientific knowledge, prior information, auxiliary sensor information, and operational constraints was done at the initialization of the PHORTEX deployment-by-deployment loop. Every trajectory generated by PHORTEX was checked by AUV *Sentry* engineers and the science team before execution. *Sentry* status was monitored with an external acoustic tracking system that monitored vehicle location, power, and performance while in acoustic range of the ship. Upon returning to deck, all science sensor observations were downloaded in bulk from the vehicle, and then ingested via our PHORTEX system.

the structure of a plume microbiome. It is typical that research cruises have several science teams working together under an appointed chief scientist to maximize the use of ship assets while at sea. To assist in operations, AUV *Sentry*, remotely-operated vehicle (ROV) *JASON*, and standard oceanographic acoustic and profiling equipment were available. The deployment of PHORTEX on the cruise for *Sentry* operations was coupled with objectives to test *in situ* instruments and collect microbiota samples. For both of these tasks, charting different regions within a plume structure was important to test the limits of the novel instruments and collect microbiota samples from a diversity of plume-conditions.

6.4.1 SITE DESCRIPTION AND GENERAL CONDITIONS

The main site for the study conducted by AUV *Sentry* using PHORTEX is a hydrothermal ridge located in the northern Guaymas Basin, approximately 1850 m underwater and at the edge of an additionally 300 m deeper graben (a valley with steep sides) (Fig. 6.5). The ridge is approximately 600 m long and features several tall sulfide structures 45-75 m in height with active smoking along their bodies. A smoking “chimney”

at the northernmost point of the ridge was targeted for plume-charting. Composed of a cluster of tens of small orifices (<0.1 m diameter) creating an approximately 1.5 m diameter chimney base, the fluid produced was thick with particulate matter, 340 °C at the source, ventilated rapidly at approximately 0.7 m s^{-1} (as measured by video equipment), and rich in dissolved methane. In contrast, the ambient seawater was methane-poor, considerably less turbid, and cold at 4 °C. Vent characteristics were measured by ROV *JASON* carrying specialized sensing equipment, and we use these measurements as a means of seeding and measuring the performance of PHUMES within PHORTEX.

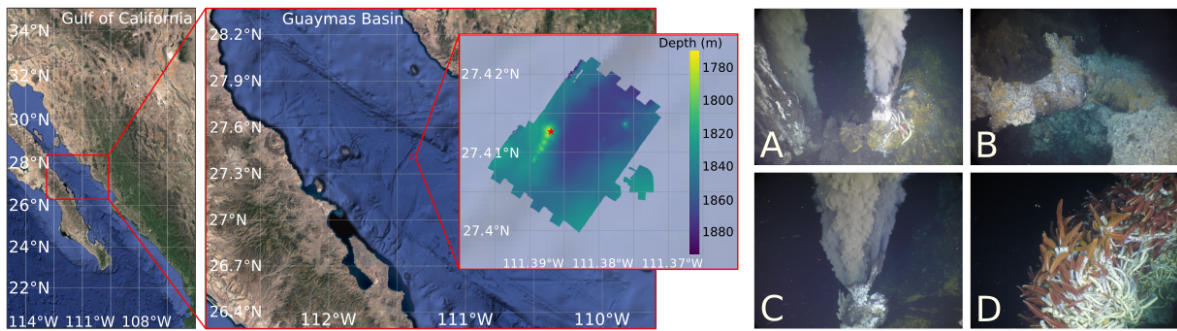


Figure 6.5: Study site in the Guaymas Basin, Gulf of California. The inset map is bathymetric data collected by AUV *Sentry* during this expedition and shows the approximately 600 m long ridge in yellow. The red star marks the chimney that was of particular study in this article. Pictures A-D show imagery from the ridge and chimney site. A-C show various forms of plume-producing vents located at the chimney and D shows an example of the macrofauna covering the structures along the ridge.

As vent fluids rise and form a plume at this site, the ambient water is mixed (entrained) at an unknown rate. The presence of advective crossflow, reaching magnitudes up to 0.1 m s^{-1} , was obvious from images of the bending plume stem at the vent sites (and was measured by the bottom-mounted tiltmeters deployed during the expedition). The magnitude and heading of the crossflow appeared to be semi-cyclic, following a pattern (albeit time-delayed) established by tidal charts produced by Centro de Investigación Científica y de Educación Superior de Ensenada (CISESE) for the time period of the expedition². Local bathymetric and other physical effects on crossflow were also qualitatively observed. Under these conditions, plume expressions could be transported several hundred meters from a known source, and would be expected to rise over 200 m in the water column. In scientific work following this expedition, plume fluids were identified from collected observations over 7 km away from known venting sites [IN PREP].

²Charts available from: www.predmar.cicese.mx/calendarios

6.4.2 OVERVIEW OF SEA TRIALS WITH AUV *Sentry*

Four deployments as part of the PHORTEX study were made with AUV *Sentry*, and represent a planning “spectrum” from fully human-designed surveys to fully PHORTEX designed. We label the four deployments as follows:

- **Dive H-Multi:** human designed, multi-task survey. This was the first deployment of *Sentry* and the survey was designed to both attempt to find plume fluids and to bathymetrically map the local basin area (the map of which would be used as part of the safety check protocol for future deployments). This dive is representative of a standard “nested” strategy, in which progressively more targeted (finer resolution) surveys are used to study areas that might be of interest. The deployment lasted 21.3 hrs and collected 76,604 observations total.
- **Dive H-Plume:** human designed, plume-charting survey. This was the second deployment of *Sentry* and the survey was hand-designed by the science party onboard the vessel to find and sample plume fluids. The science party had access to the performance of *Sentry* in Dive H-Multi. The strategy was to sweep the basin above areas with known hydrothermal vents, and fly out into the basin in the direction that the plume fluids would be expected to advect. The deployment lasted 21 hrs and collected 75,430 observations total.
- **Dive HP-Plume:** hybrid human and PHORTEX plume-charting survey. This was the third deployment of *Sentry* and the survey consisted of trajectories designed by PHORTEX trained by observations collected in Dive H-Multi. Two of the trajectory primitives designed by PHORTEX were replaced by “naive” lawnmowers placed over the known vent at two different times in the deployment. The deployment lasted 22.2 hrs and collected 79,792 observations total. Of these, 8.2 hrs and 29438 observations were collected via the naive strategy.
- **Dive P-Plume:** PHORTEX plume-charting survey. This was the fourth and last deployment of *Sentry*. The survey was fully designed by PHORTEX using observations from Dive H-Multi. The deployment lasted 9.9 hrs and collected 35,755 observations total. This deployment is notably much shorter than the other deployments due to increasing time constraints as the expedition was coming to a close. This deployment also used *Sentry*’s depth hold mode; whereas in all other dives *Sentry*’s depth followed the basin terrain, in this experiment the robot held an absolute depth.

6.4.3 EXPERIMENTAL RESULTS

We look at several key metrics for each deployment: proportion of positive plume observations, utilization of spatial extent, and utilization of temporal window. The first metric, proportion of positive plume observations, is simply the number of observations collected in a dive that were classified as in-plume by the binary psuedo-sensor we describe in Section 6.3.1. The second metric attempts to show how effective the design of the survey was spatially by first showing the absolute range that positive detections were made as a measure of distance from the chimney vent location and second showing how that range fit with the overall design of the survey. For example, if detections were made up to 300 m away from the vent, but the robot traveled up to 1 km away, then the survey spent too much time outside of the detectable plume region and would not be as effective as a survey that only traveled 200 m away but stayed well within the detectable plume range. Finally, the last metric is a measure of how effective the survey was at *staying* or *revisiting* a plume over time. Given the duration of these missions, it is important to use the entire mission window for the task at hand; moreover temporally “diverse” observations are of scientific interest generally. We report the dive hours with at least 10% or more positive detections.

A summary of these metrics for each dive is provided in Table 6.2 and visualized in Fig. 6.6. In general, we see that PHORTEX performs as least as well as the human-designed surveys in terms of total number of samples collected, while improving spatial utilization (both with respect to effective utilization of the entire explored range, and in terms of increasing the effective detection range over naive trajectories placed “on top” of the vent). Absolute temporal utilization is similar to human surveys, however the distribution of detections within the temporal utilization windows is potentially improved—for human surveys, detections tend to be “bunched” to either the first half (as in H-Plume) or second half (as in H-Multi). Anecdotally, in HP-Plume, the two human-designed surveys occur in hours 5-8 and 20-23. While there were detections in both of these windows, over 90% of total positive detections by these trajectories were collected only in the window from hours 20-23; in contrast the proportion of positive samples in the PHORTEX designed trajectories in HP-Plume were more uniformly distributed in time (approximately 40% collection in each window).

In this field deployment it is obvious that PHORTEX could be a useful tool for plume-charting. The performance of trajectories designed with PHORTEX are comparable to those designed by humans with key possible improvements in spatial and temporal utilization. Moreover, the automated nature of PHORTEX operationally alleviates sig-

Dive	Duration	Total Obs.	Prop. In-Plume	Spatial Util.	Temporal Util.
H-Multi	21.3 hrs	76,604	22.3%	300 m (19%)	9-17,20-21 (52%)
H-Plume	21 hrs	75,430	10.9%	900 m (64%)	2,5-8,10-11,15-16 (43%)
HP-Plume	22.2 hrs	79,792	41.8%	600 m (100%)	1-3,5,7,11-23 (81%)
HP-Plume (H)	8.2 hrs	29,438	42.3%	250 m (100%)	5,7,20-23 (75%)
HP-Plume (P)	14 hrs	50,354	41.5%	600 m (100%)	1-3,11-20 (93%)
P-Plume	9.9 hrs	35,755	12.8%	450 m (100%)	1,5,8,9 (40%)

Table 6.2: Per-deployment statistics for field trials of PHORTEX. The deployment HP-Plume is broken further into human designed (H) and PHORTEX designed (P) portions for direct comparison.

nificant decision-making burden on a science team and the trajectory-design burden on the *Sentry* team; the ability to ingest data from external sensors and previous *Sentry* missions, and produce trajectories that can be seamlessly ingested by the safety checking system without human intervention is of considerable benefit when actually in the field. Moreover, the intermediate products of PHORTEX, such as PHUMES forecasts, are operationally useful for other tasks in field operations, such as deploying other instruments or prioritizing instrument deployment order based on temporal changes in the environment.

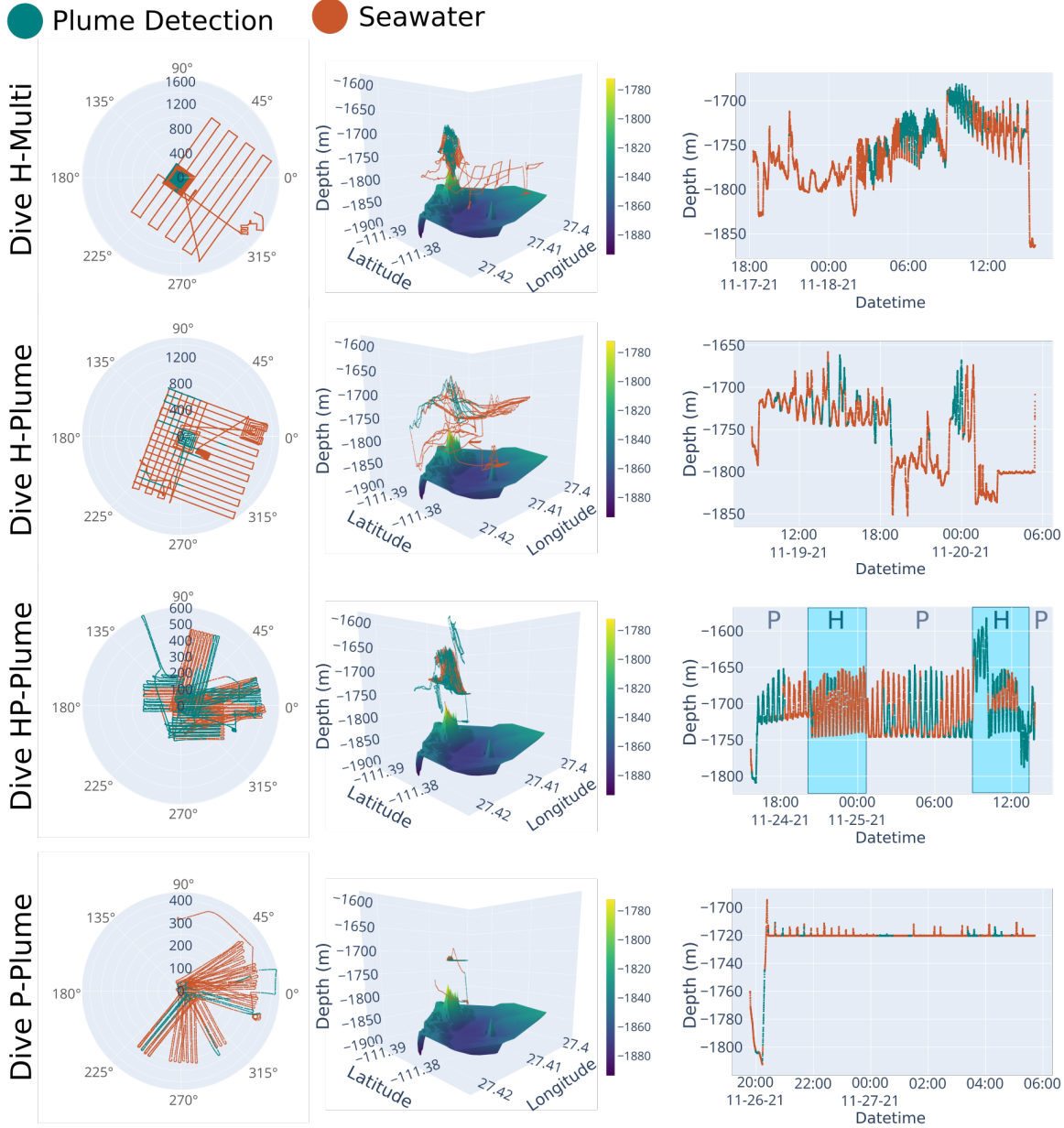


Figure 6.6: The four field dives of AUV *Sentry*. All data is plotted according to its detection identity (in-plume or seawater). The first column shows a top-view of the dive trajectories in polar coordinates, in which angle and radius is computed relative to the chimney coordinate of the vent of study. In the center column, the 3D path of the vehicle over the rendered bathymetric terrain is provided. All but Dive P-Plume were dives conducted in altitude-hold mode with *Sentry*, and so the trajectories show obvious changes in elevation; in contrast Dive P-Plume was held in depth-hold mode, so most observations are gathered within a depth-plane. The final column shows a time series versus depth of the detections collected. In Dive HP-Plume the portions of the dive that were human-designed and PHORTEX-designed are labeled with H and P, respectively. As can be seen in the Dive HP-Plume time series, the two human-designed trajectories have significantly different performance, despite being in locally similar regions of the spatial domain.

7

PLANNING: ADAPTIVE SAMPLING IN SPATIOTEMPORAL FIELDS

7.1 UNDERWAY AUTONOMY: PLUMES

7.2 DEPLOYMENT-BY-DEPLOYMENT AUTONOMY:
PHORTEX

7.3 FIELD RESULTS IN GB

7.4 SUMMARY

8 DISCUSSION

8.1 GENERALIZING TO OTHER DOMAINS

8.2 OPEN CHALLENGES

8.3 EMBEDDING AUTONOMY ENGINEERS INTO SCIENCE
TEAMS

8.4 ROBOTICS IN EXPEDITIONARY SCIENCE

9 LOOKING FORWARD

This is the conclusion section.

A PERCEIVING

A.1 METHOD FOR METHANE MEASUREMENT FROM NISKIN BOTTLES

A Los Gatos Research (LGR) Dissolved Gas Extraction Unit (DGEU) and Greenhouse Gas Analyzer (GGA) were used to process water collected by Niskin bottle samples during the transect, and report methane concentration estimates to be compared to the *in situ* observation of normalized methane by SAGE mounted on the rosette. Measurements of methane made by the GGA are reported as the stabilized parts per million (ppm) reading provided by the instrument after consuming 3-5 L of seawater from each Niskin bottle, and are converted to nanomolar (nM) values by first computing the partial pressure of methane, and then computing molarity by estimating the solubility constant of methane using coincident measurements of salinity and temperature of the seawater at time of bottle sample collection as measured by the rosette CTD. The conversion from partial pressure to molarity is done using the `gasex` Python library, publicly hosted at <https://github.com/boom-lab/gasex-python>.

To transform GGA measurements in ppm to partial pressure, the DGEU cell pressure is used, such that $\text{ppm} \times \text{cell pressure} = \text{partial pressure}$. Additionally, gas extraction inefficiency is taken into consideration at this step; the DGEU does not perfectly extract gas across the membrane during sampling. Extraction efficiency is used to scale the GGA measurement of methane prior to computing the partial pressure estimate by

$$\left[\frac{x_{obs} - x_{ref}}{\lambda_{eff}} + x_{ref} \right] \frac{p_{cell}}{1000} = x_{pp} \quad (\text{A.1})$$

where x_{obs} is the ppm measurement made by the GGA, x_{ref} is a methane reference value (the atmospheric concentration of methane, typically between 1.86-1.99 ppm), λ_{eff} is the extraction efficiency, p_{cell} is the cell pressure in millibar, and x_{pp} is the estimated partial pressure value, in μatm .

The extraction efficiency used in this manuscript was estimated by laboratory calibrations to be between 2.3-3.3%, consistent across different water temperatures and different test tank concentrations. In the laboratory calibration procedure, methane was bubbled in a temperature-controlled tank which was stirred before two discrete samples were taken using 60 mL syringes filled with 40 mL of water, and 20 mL of pure nitrogen gas. A DGEU, connected to the GGA, was then used to take water from the target tank, and ppm measurements by the GGA were recorded when measurements stabilized; this was done with two different DGEUs, which we label A and B. To estimate “ground truth” partial pressure of methane in the tank, the syringe samples were shaken for 2 minutes to extract the dissolved gas content, and the water drained. The samples were then processed within 24 hours on a gas chromatography instrument (Shimadzu GC-14B), run alongside a set of standards processed every 5 minutes. The measurements from the processed syringes (DGEU influent) were used as x_{pp} in Eq. A.1, the GGA observations as x_{obs} , the value 1.99 ppm used as x_{ref} , and 495 mbar as p_{cell} . The relevant data from these calibrations is available in Tab. A.1. DGEU A was the instrument used in the transect field mission as presented in this manuscript.

DGEU	Temperature (C)	Influent (μatm)	GGA Methane (ppm)	Efficiency
A	4.7	299.13	21.82	3.29%
A	4.7	512.03	6.44	0.4%
A	4.7	588.25	41.04	3.29%
B	4.7	299.13	17.77	2.62%
B	4.7	512.03	25.68	2.29%
B	4.7	588.25	30.09	2.37%
A	9.9	267.14	17.02	2.80%
A	9.9	403.45	27.84	3.18%
A	9.9	856.89	55.77	3.11%
B	9.9	267.14	12.72	2.00%
B	9.9	403.45	18.63	2.05%
B	9.9	856.89	36.99	2.02%
A	14.8	18.64	2.78	2.22%
A	14.8	1549.18	101.26	3.17%
A	14.8	1640.81	100.41	2.97%
B	14.8	18.64	2.63	1.80%
B	14.8	1549.18	78.93	2.46%
B	14.8	1640.81	68.43	2.01%

Table A.1: Results of DGEU extraction efficiency calibration experiments.

A.2 LEG 2 NISKIN BOTTLE SAMPLE SCHEDULE AND MEASUREMENTS

This manuscript presents methane and ammonium measurements collected by Niskin bottles during Leg 2 of the rosette trajectory. Table A.2 provides the schedule of Niskin bottle firing performed during Leg 2, and Table A.3 provides all data associated with those bottles collected and presented in Chapter 3 of this thesis. The range of methane nM values is provided by converting GGA methane ppm measurements as described in Sec. A.1 for the conservative range of valid DGEU extraction efficiency values.

Bottle	Time	Location	Depth (m)
1	2021-11-30 09:10:03	27.3951N 111.3649W	1648.62
3	2021-11-30 09:30:03	27.3956N 111.3665W	1625.67
5	2021-11-30 09:47:01	27.3967N 111.3696W	1639.25
7	2021-11-30 09:47:05	27.3967N 111.3696W	1639.05
9	2021-11-30 10:07:00	27.3985N 111.3740W	1598.32
11	2021-11-30 10:17:02	27.2994N 111.3765W	1580.5
13	2021-11-30 10:27:01	27.4005N 111.3791W	1568.27
15	2021-11-30 10:27:04	27.4005N 111.3791W	1568
17	2021-11-30 10:37:20	27.4016N 111.2818W	1558.64
19	2021-11-30 10:46:59	27.4027N 111.3845W	1553.92
21	2021-11-30 11:07:05	27.4051N 111.3900W	1547
23	2021-11-30 11:33:00	27.4082N 111.3971W	1545.4

Table A.2: Schedule of bottle samples during Leg 2 of rosette trajectory.

A.3 NORMALIZED PYTHIA CALIBRATION

The Pythia instrument provides a significantly nonlinear output reference value when measuring methane. We correct for this nonlinearity using a reference curve computed in the laboratory before normalizing the measurements as reported in this manuscript. The reference curve was created using a temperature-fixed (3 °C) tank and closed equilibration chamber, in which methane standards were bubbled until fully equilibrated before being measured by the instrument. Stable measurements by Pythia (which has a response time of approximately 35 minutes) were then recorded at different chamber

Bottle	CH ₄ (ppm)	CH ₄ (nM)	NH ₄ ⁺ (nM)	Temp. (C)	Salinity (PSU)
1	—	—	0.00	2.8334	34.6104
3	9.29	207-296	46.35	2.8578	35.6095
5	21.6	547-785	—	2.8458	34.6107
7	—	—	174.48	2.8461	34.6108
9	22.54	573-821	165.99	2.8659	34.6101
11	29.82	774-1110	225.87	2.8719	34.6096
13	44.36	1176-1686	—	2.8734	34.6099
15	—	—	384.28	2.8733	34.6098
17	89.45	2421-3473	780.53	2.8849	34.6105
19	114.27	3105-4454	997.45	2.8968	34.6111
21	27.29	704-1009	227.54	2.8835	34.6087
23	11.5	268-384	89.29	2.8964	34.6075

Table A.3: Geochemical measurements associated with the schedule of bottle samples during Leg 2 of rosette trajectory. Note that methane expressed in nM is computed using coincident temperature and salinity measurements during the transect as measured by rosette CTD, and extraction inefficiency of the DGEU is compensated for as described in Sec. A.1.

concentrations. The calibration curve that results is a piece-wise linear function, shown in Fig. A.1.

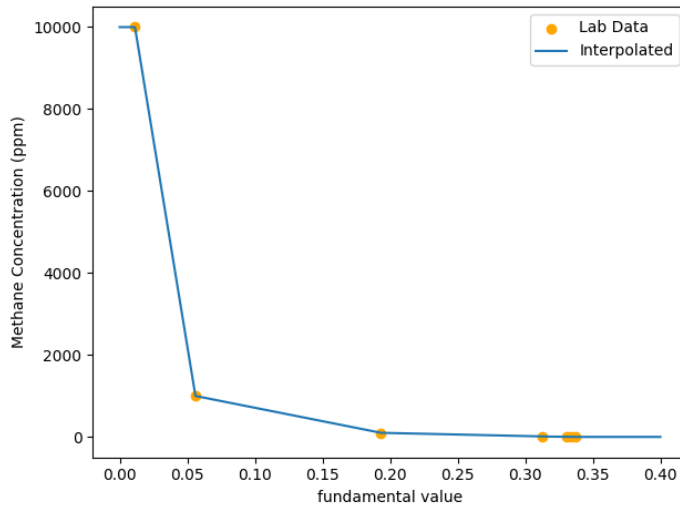


Figure A.1: Fitted calibration curve for measurements of methane observed by Pythia.

Compensation of Pythia's time response was also performed on post-calibrated data using the methodology described in [76] with a smoothing window of 5 minutes, and

subsampling at a quarter of the time delay window. This methodology is sensitive to noise in the signal, which motivates the extreme sub-sampling that is performed. Fig. A.2 shows the effect of smoothing, time-correction, and conversion on the direct signal recorded by Pythia before normalization.

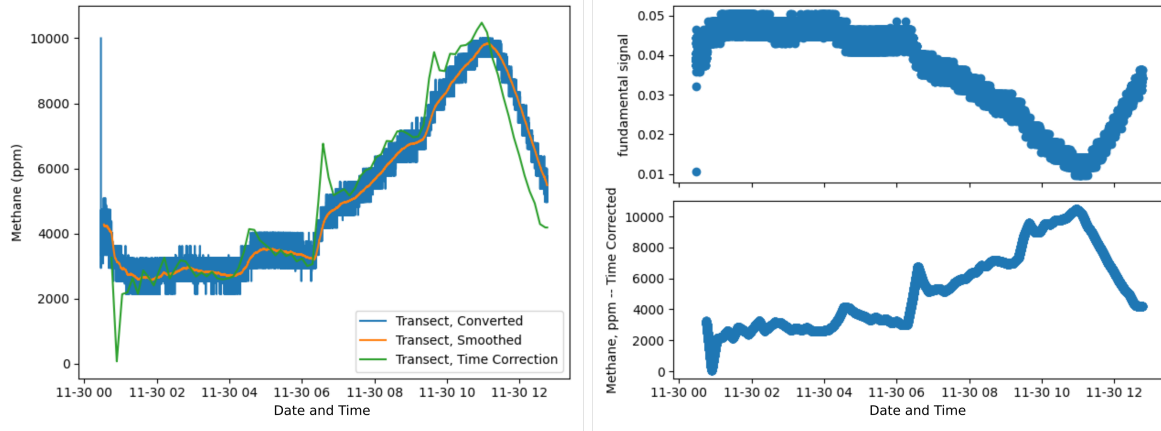


Figure A.2: Calibration curve, smoothing, and time correction applied to Pythia observations during the transect, before reported normalization in the manuscript.

A.4 DEPTH-CORRECTION

Temperature, salinity, and oxygen are expected to be weakly stratified in the deep ocean. To remove these effects from data collected by AUV Sentry and the rosette, we fit a line to the average observations collected within binned 20 m intervals of observed depth for each platform separately. Separately computing the correction for each instrument additionally controls for small discrepancies in calibration between the platforms. Fig. A.3 compares these lines with the observations collected.

A.5 DESCRIPTION OF PLUME MODEL FOR TRANSECT DESIGN

We adapted an idealized buoyant bent-plume model proposed by [35] for atmospheric bent plumes in a weakly stratified fluid in order to inform at what heights to deploy AUV Sentry and the rosette during the transect. We rewrite the system of equations provided in [35] as follows:

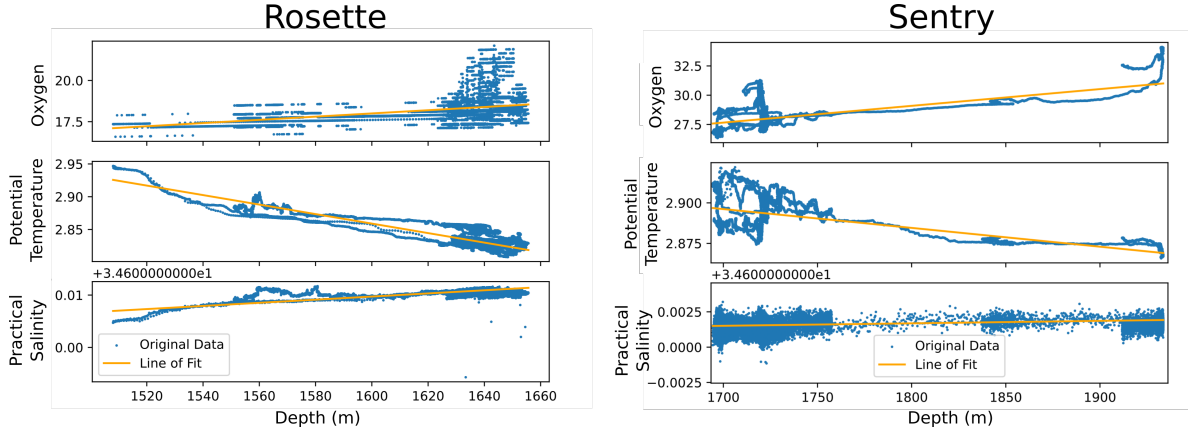


Figure A.3: Linear functions are fit to data collected for oxygen, temperature, and salinity instruments on each platform separately. A residual value is then computed for each observation.

$$E = \alpha \left| \frac{M}{Q} - u \cos(\theta) \right| + \beta |u \sin(\theta)| \quad (\text{A.2})$$

$$\frac{dQ}{ds} = Q E \sqrt{\frac{2(1 + \lambda^2)}{M \lambda}} \quad (\text{A.3})$$

$$\frac{dM}{ds} = u \cos(\theta) \frac{dQ}{ds} + \frac{FQ}{M} \sin(\theta) \quad (\text{A.4})$$

$$\frac{d\theta}{ds} = \left(\frac{FQ}{M} \cos(\theta) - u \sin(\theta) \frac{dQ}{ds} \right) \frac{1}{M} \quad (\text{A.5})$$

$$\frac{dF}{ds} = -QN^2 \sin(\theta) \quad (\text{A.6})$$

$$\frac{dX}{ds} = \cos(\theta) \quad (\text{A.7})$$

$$\frac{dZ}{ds} = \sin(\theta) \quad (\text{A.8})$$

where E is a mixing entrainment coefficient which considers both vertical and horizontal mixing and is weighted by parameters α and β , u is the crossflow velocity which can be a function of depth and time, λ is a parameter which modifies the ellipse which describes the plume envelope, Q is specific volume flux, M is specific momentum flux, F is specific buoyancy flux, θ is plume centerline trajectory angle, s is the plume centerline trajectory, X is distance along a coordinate axis aligned with the plume centerline, Z is height with respect to plume source along a vertical axis, and N^2 is the Brunt-Väisälä

frequency, computed with respect to the density gradient at the reference depths of the source and plume height.

The system of equations essentially yields a “snapshot” of a plume envelope at some moment in time. For time-varying crossflows, multiple snapshots can be computed for different moments in time (different crossflow orientations and magnitudes) and chained together in a common coordinate reference system in order to track a plume trajectory. For the purposes of determining which heights to deploy AUV Sentry and the rosette for the transect, we compute a prototypical envelope and use the estimated bent nonbuoyant plume height to set the transect depths/altitudes.

The initial conditions for solving this system of ordinary differential equations are set via estimates of vent characteristics including exit velocity, temperature, salinity, and area. Specifically:

$$Q_o = \lambda V_v \frac{A_v}{\pi} \quad (\text{A.9})$$

$$M_o = Q_o V_v \quad (\text{A.10})$$

$$F_o = -g10^{-4}(T_v - T_z)Q_o \quad (\text{A.11})$$

$$\theta_o = \frac{\pi}{2} \quad (\text{A.12})$$

where V_v is exit velocity at the vent orifice, A_v is the vent orifice area, T_v is the temperature at the orifice area, and T_z is the expected temperature of ambient seawater at the estimated vent depth. Note that initial buoyancy flux is primarily driven by temperature changes, as we anticipate this to be the major driver of density gradients at our measurement scale. Expected salinity gradients could be similarly considered.

Estimated vent characteristics and crossflow were selected based on empirical observations of the deep sea vents located along the northern Guaymas Basin ridge and observations of current magnitude collected by a current tiltmeter deployed by ROV Jason during several days of the research cruise. Table A.4 lists the settings for planning the transect selected for these characteristics. Background salinity and temperature profiles were computed according to standard Pacific Ocean temperature and salinity functions as described in [18]; additionally the equation of state for computing density profile from salinity and temperature measurements was used also as defined in [18]. The prototypical plume is computed with a source located at 1850 m depth.

The prototypical plume envelope computed in this manner estimates a nonbuoyant plume depth between 1570-1750 m (Fig. A.4). AUV Sentry is altitude limited in order

Parameter	Assignment	Description
λ	1.0	Ratio of elliptical axes of the plume envelope
V_v	0.58 m s^{-1}	Exit velocity of fluids at vent orifice
A_v	0.82 m^2	Area of vent orifice
T_v	340°C	Temperature of fluids at vent orifice
α	0.15	Longitudinal shear-driven mixing coefficient
β	0.19	Transverse shear-driven mixing coefficient
u	0.1 m s^{-1}	Magnitude of crossflow

Table A.4: Parameter, vent characteristics, and ambient crossflow setting used for transect design.

to keep a fix on the ocean floor for navigation; it is set to its maximum altitude of 120 m in order to intersect with the bottom of the estimated nonbuoyant layer; this corresponds to a depth of approximately 1700 m throughout the basin. The rosette can be arbitrarily fixed to a height, but so as not to interfere with AUV Sentry operations and to sample a different point in the estimated nonbuoyant layer, a depth of 1650-1600 m was targeted.

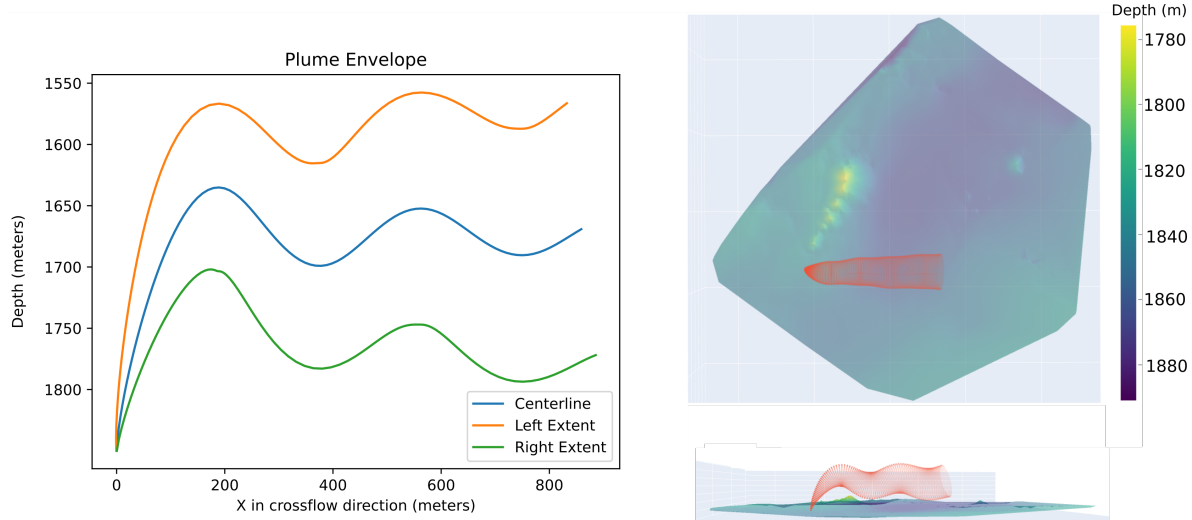


Figure A.4: A prototypical plume estimate according to the modified buoyant plume model in crossflow. The same envelope is plotted with respect to absolute depth (with a source located at 1850 m) on the left, and illustratively in the context of the hydrothermal ridge on the right.

ACRONYMS

POMDP Partially-observable Markov decision-process

GLOSSARY

L^AT_EX A document preparation system

BIBLIOGRAPHY

1. R. Camilli, C. M. Reddy, D. R. Yoerger, B. A. Van Mooy, M. V. Jakuba, J. C. Kinsey, C. P. McIntyre, S. P. Sylva, and J. V. Maloney, “Tracking hydrocarbon plume transport and biodegradation at deepwater horizon,” *Science*, vol. 330:no. 6001, 2010.
2. G. Flaspohler, V. Preston, A. P. Michel, Y. Girdhar, and N. Roy, “Information-guided robotic maximum seek-and-sample in partially observable continuous environments,” *IEEE Robotics and Automation Letters*, 2019.
3. S. Särkkä, *Bayesian filtering and smoothing*, 3. Cambridge university press, 2013.
4. G. Welch, G. Bishop, *et al.*, “An introduction to the kalman filter,” 1995.
5. D. Silver and J. Veness, “Monte-Carlo planning in large POMDPs,” in *Proc. Adv. Neural Inf. Process. Syst.*, 2010.
6. V. Preston, G. Flaspohler, J. Kapit, W. Pardis, S. Youngs, D. E. Martocello III, N. Roy, P. R. Girguis, S. D. Wankel, and A. P. M. Michel, “Discovering hydrothermalism from afar: In situ methane instrumentation and change-point detection for decision-making,” *Frontiers in Earth Science*, 2022.
7. J. B. Corliss, J. Dymond, L. I. Gordon, J. M. Edmond, R. P. von Herzen, R. D. Ballard, K. Green, D. Williams, A. Bainbridge, K. Crane, *et al.*, “Submarine thermal springs on the galapagos rift,” *Science*, vol. 203:no. 4385, 1979.
8. S. E. Beaulieu, E. T. Baker, and C. R. German, “Where are the undiscovered hydrothermal vents on oceanic spreading ridges?” *Deep Sea Research Part II: Topical Studies in Oceanography*, vol. 121, 2015.
9. N. Le Bris, M. Yücel, A. Das, S. M. Sievert, P. LokaBharathi, and P. R. Girguis, “Hydrothermal energy transfer and organic carbon production at the deep seafloor,” *Frontiers in Marine Science*, vol. 5, 2019.

10. J. A. Resing, P. N. Sedwick, C. R. German, W. J. Jenkins, J. W. Moffett, B. M. Sohst, and A. Tagliabue, “Basin-scale transport of hydrothermal dissolved metals across the South Pacific Ocean,” *Nature*, vol. 523:no. 7559, 2015.
11. G. J. Dick, K. Anantharaman, B. J. Baker, M. Li, D. C. Reed, and C. S. Sheik, “The microbiology of deep-sea hydrothermal vent plumes: Ecological and biogeographic linkages to seafloor and water column habitats,” *Frontiers in Microbiology*, vol. 4, 2013.
12. C. Vic, J. Gula, G. Roullet, and F. Pradillon, “Dispersion of deep-sea hydrothermal vent effluents and larvae by submesoscale and tidal currents,” *Deep Sea Research Part I: Oceanographic Research Papers*, vol. 133, 2018.
13. F. Scholz, M. Schmidt, C. Hensen, S. Eroglu, S. Geilert, M. Gutjahr, and V. Liebetrau, “Shelf-to-basin iron shuttle in the Guaymas Basin, Gulf of California,” *Geochimica et Cosmochimica Acta*, vol. 261, 2019.
14. J. B. Bell, C. Woulds, and D. v. Oevelen, “Hydrothermal activity, functional diversity and chemoautotrophy are major drivers of seafloor carbon cycling,” *Scientific reports*, vol. 7:no. 1, 2017.
15. J. F. Grassle, “The ecology of deep-sea hydrothermal vent communities,” in *Advances in Marine Biology*, vol. 23, Elsevier, 1987.
16. M. N. Georgieva, C. T. Little, V. V. Maslennikov, A. G. Glover, N. R. Ayupova, and R. J. Herrington, “The history of life at hydrothermal vents,” *Earth-Science Reviews*, vol. 217, 2021.
17. B. Morton, G. I. Taylor, and J. S. Turner, “Turbulent gravitational convection from maintained and instantaneous sources,” *Proceedings of the Royal Society of London. Series A. Mathematical and Physical Sciences*, 1956.
18. K. G. Speer and P. A. Rona, “A model of an atlantic and pacific hydrothermal plume,” *Journal of Geophysical Research: Oceans*, vol. 94:no. C5, 1989.
19. C. S. Chin, K. H. Coale, V. A. Elrod, K. S. Johnson, G. J. Massoth, and E. T. Baker, “In situ observations of dissolved iron and manganese in hydrothermal vent plumes, Juan de Fuca ridge,” *Journal of Geophysical Research: Solid Earth*, vol. 99:no. B3, 1994.

20. S. A. Bennett, M. Coleman, J. A. Huber, E. Reddington, J. C. Kinsey, C. McIntyre, J. S. Seewald, and C. R. German, “Trophic regions of a hydrothermal plume dispersing away from an ultramafic-hosted vent-system: Von Damm vent-site, Mid-Cayman Rise,” *Geochemistry, Geophysics, Geosystems*, vol. 14:no. 2, 2013.
21. J. S. Seewald, W. E. Seyfried Jr, and W. C. Shanks III, “Variations in the chemical and stable isotope composition of carbon and sulfur species during organic-rich sediment alteration: an experimental and theoretical study of hydrothermal activity at Guaymas Basin, Gulf of California,” *Geochimica et Cosmochimica Acta*, vol. 58:no. 22, 1994.
22. K. Von Damm, J. t. Edmond, C. Measures, and B. Grant, “Chemistry of submarine hydrothermal solutions at Guaymas Basin, Gulf of California,” *Geochimica et Cosmochimica Acta*, vol. 49:no. 11, 1985.
23. H. Ondréas, C. Scalabrin, Y. Fouquet, and A. Godfroy, “Recent high-resolution mapping of Guaymas hydrothermal fields (Southern Trough),” *Bulletin de la Société Géologique de France*, vol. 189:no. 1, 2018.
24. A. Teske, D. De Beer, L. J. McKay, M. K. Tivey, J. F. Biddle, D. Hoer, K. G. Lloyd, M. A. Lever, H. Røy, D. B. Albert, *et al.*, “The Guaymas Basin hiking guide to hydrothermal mounds, chimneys, and microbial mats: Complex seafloor expressions of subsurface hydrothermal circulation,” *Frontiers in Microbiology*, vol. 7, 2016.
25. P. Lonsdale and K. Becker, “Hydrothermal plumes, hot springs, and conductive heat flow in the Southern Trough of Guaymas Basin,” *Earth and Planetary Science Letters*, vol. 73:no. 2-4, 1985.
26. S. A. Soule, J. Seewald, S. D. Wankel, A. Michel, R. Beinart, E. E. Briones, E. M. Dominguez, P. Girguis, D. Coleman, N. A. Raineault, *et al.*, “Exploration of the Northern Guaymas Basin,” *Oceanography*, vol. 31:no. 1, 2018.
27. S. Geilert, C. Hensen, M. Schmidt, V. Liebetrau, F. Scholz, M. Doll, L. Deng, A. Fiskal, M. A. Lever, C.-C. Su, *et al.*, “On the formation of hydrothermal vents and cold seeps in the Guaymas Basin, Gulf of California,” *Biogeosciences*, vol. 15:no. 18, 2018.
28. A. P. Michel, V. L. Preston, K. E. Fauria, and D. P. Nicholson, “Observations of shallow methane bubble emissions from Cascadia margin,” *Frontiers in Earth Science*, vol. 9, 2021.

29. R. M. Holmes, A. Aminot, R. Kérouel, B. A. Hooker, and B. J. Peterson, “A simple and precise method for measuring ammonium in marine and freshwater ecosystems,” *Canadian Journal of Fisheries and Aquatic Sciences*, vol. 56:no. 10, 1999.
30. B. W. Taylor, C. F. Keep, R. O. Hall Jr, B. J. Koch, L. M. Tronstad, A. S. Flecker, and A. J. Ulseth, “Improving the fluorometric ammonium method: Matrix effects, background fluorescence, and standard additions,” *Journal of the North American Benthological Society*, vol. 26:no. 2, 2007.
31. J. Kapit and A. P. Michel, “Dissolved gas sensing using an anti-resonant hollow core optical fiber,” *Applied Optics*, vol. 60:no. 33, 2021.
32. ——, “Measurement of dissolved gases using a hollow core optical fiber and capillary membrane inlet,” in *CLEO: Applications and Technology*, Optical Society of America, 2021.
33. A. P. Michel, J. Kapit, B. Colson, W. Pardis, V. Preston, S. Youngs, L. Uecker, R. Ruwini, Z. Moya, J. Roberts, T. Rawson, P. Hemp, C. Harb, S. Wankel, and G. Flaspohler, “Gas sensing in the deep ocean: Advancing our ability to chemically explore,” Ocean Science Meeting 2022, 2022.
34. C. C. Harb, T. K. Boyson, A. G. Kallapur, I. R. Petersen, M. E. Calzada, T. G. Spence, K. P. Kirkbride, and D. S. Moore, “Pulsed quantum cascade laser-based CRDS substance detection: real-time detection of TNT,” *Opt. Express*, vol. 20:no. 14, 2012. DOI: [10.1364/OE.20.015489](https://doi.org/10.1364/OE.20.015489).
35. A. Tohidi and N. B. Kaye, “Highly buoyant bent-over plumes in a boundary layer,” *Atmospheric Environment*, vol. 131, 2016.
36. R. A. Feely, G. J. Massoth, E. T. Baker, G. T. Lebon, and T. L. Geiselman, “Tracking the dispersal of hydrothermal plumes from the Juan de Fuca Ridge using suspended matter compositions,” *Journal of Geophysical Research: Solid Earth*, vol. 97:no. B3, 1992.
37. D. R. Yoerger, A. M. Bradley, M. Jakuba, C. R. German, T. Shank, and M. Tivey, “Autonomous and remotely operated vehicle technology for hydrothermal vent discovery, exploration, and sampling,” *Oceanography*, vol. 20:no. 1, 2007.
38. N. Bray, “Water mass formation in the Gulf of California,” *Journal of Geophysical Research: Oceans*, vol. 93:no. C8, 1988.

39. M. V. Jakuba, "Stochastic mapping for chemical plume source localization with application to autonomous hydrothermal vent discovery," PhD thesis, Massachusetts Institute of Technology, 2007.
40. J. P. Cowen, X. Wen, and B. N. Popp, "Methane in aging hydrothermal plumes," *Geochimica et Cosmochimica Acta*, vol. 66:no. 20, 2002.
41. A. Branch, J. McMahon, G. Xu, M. V. Jakuba, C. R. German, S. Chien, J. C. Kinsey, A. D. Bowen, K. P. Hand, and J. S. Seewald, "Demonstration of autonomous nested search for local maxima using an unmanned underwater vehicle," in *2020 IEEE International Conference on Robotics and Automation (ICRA)*, IEEE, 2020.
42. L. Wang, S. Pang, and G. Xu, "3-dimensional hydrothermal vent localization based on chemical plume tracing," in *Global Oceans 2020: Singapore–US Gulf Coast*, IEEE, 2020.
43. C. L. Kaiser, D. R. Yoerger, J. C. Kinsey, S. Kelley, A. Billings, J. Fujii, S. Suman, M. Jakuba, Z. Berkowitz, C. R. German, *et al.*, "The design and 200 day per year operation of the autonomous underwater vehicle sentry," in *2016 IEEE/OES Autonomous Underwater Vehicles (AUV)*, IEEE, 2016.
44. G. Hitz, E. Galceran, M.-È. Garneau, F. Pomerleau, and R. Siegwart, "Adaptive continuous-space informative path planning for online environmental monitoring," *J. Field Robot.*, vol. 34:no. 8, 2017.
45. G. A. Hollinger and G. S. Sukhatme, "Sampling-based motion planning for robotic information gathering," in *Proc. Robot. Sci. Syst.*, Citeseer, vol. 3, 2013.
46. D. Levine, B. Luders, and J. How, "Information-rich path planning with general constraints using rapidly-exploring random trees," in *AIAA Infotech at Aerospace 2010*, AIAA, 2010.
47. J. Binney and G. S. Sukhatme, "Branch and bound for informative path planning," in *Proc. IEEE Int. Conf. Robot. Autom.*, 2012.
48. A. Krause, A. Singh, and C. Guestrin, "Near-optimal sensor placements in gaussian processes: Theory, efficient algorithms and empirical studies.,," *Journal of Machine Learning Research*, vol. 9:no. 2, 2008.
49. Z. Wang, H.-X. Li, and C. Chen, "Reinforcement learning-based optimal sensor placement for spatiotemporal modeling," *IEEE transactions on cybernetics*, vol. 50:no. 6, 2019.

50. Z. N. Sunberg and M. J. Kochenderfer, “Online algorithms for POMDPs with continuous state, action, and observation spaces,” in *Proc. 24th Int. Conf. Automated Plan. Schedul.*, 2018.
51. A. Somani, N. Ye, D. Hsu, and W. S. Lee, “DESPOT: Online POMDP planning with regularization,” in *Proc. Adv. Neural Inf. Process. Syst.*, 2013.
52. L. Kocsis and C. Szepesvári, “Bandit based monte-carlo planning,” in *Proc. Euro. Conf. Mach. Learn.*, Springer, 2006.
53. H. W. Jannasch and M. J. Mottl, “Geomicrobiology of deep-sea hydrothermal vents,” *Science*, vol. 229:no. 4715, 1985.
54. W. Martin, J. Baross, D. Kelley, and M. J. Russell, “Hydrothermal vents and the origin of life,” *Nature Reviews Microbiology*, vol. 6:no. 11, 2008.
55. K. McGill and S. Taylor, “Robot algorithms for localization of multiple emission sources,” *ACM Computing Surveys (CSUR)*, vol. 43:no. 3, 2011.
56. K. Nakamura, T. Toki, N. Mochizuki, M. Asada, J.-i. Ishibashi, Y. Nogi, S. Yoshikawa, J.-i. Miyazaki, and K. Okino, “Discovery of a new hydrothermal vent based on an underwater, high-resolution geophysical survey,” *Deep Sea Research Part I: Oceanographic Research Papers*, vol. 74, 2013.
57. J. B. Paduan, R. A. Zierenberg, D. A. Clague, R. M. Spelz, D. W. Caress, G. Troni, H. Thomas, J. Glessner, M. D. Lilley, T. Lorenson, *et al.*, “Discovery of hydrothermal vent fields on alarcón rise and in southern pescadero basin, gulf of california,” *Geochemistry, Geophysics, Geosystems*, vol. 19:no. 12, 2018.
58. J. C. Mason, A. Branch, G. Xu, M. V. Jakuba, C. R. German, S. Chien, A. D. Bowen, K. P. Hand, and J. S. Seewald, “Evaluation of auv search strategies for the localization of hydrothermal venting,” 2020.
59. J. Kim, S.-K. Son, D. Kim, S.-J. Pak, O. H. Yu, S. L. Walker, J. Oh, S. K. Choi, K. Ra, Y. Ko, *et al.*, “Discovery of active hydrothermal vent fields along the central indian ridge, 8–12° s,” *Geochemistry, Geophysics, Geosystems*, vol. 21:no. 8, 2020.
60. G. Ferri, M. V. Jakuba, and D. R. Yoerger, “A novel trigger-based method for hydrothermal vents prospecting using an autonomous underwater robot,” *Autonomous Robots*, vol. 29:no. 1, 2010.
61. S. E. Beaulieu, E. T. Baker, C. R. German, and A. Maffei, “An authoritative global database for active submarine hydrothermal vent fields,” *Geochemistry, Geophysics, Geosystems*, vol. 14:no. 11, 2013.

62. G. Reddy, V. N. Murthy, and M. Vergassola, “Olfactory sensing and navigation in turbulent environments,” *Annual Review of Condensed Matter Physics*, vol. 13, 2022.
63. X.-x. Chen and J. Huang, “Odor source localization algorithms on mobile robots: A review and future outlook,” *Robotics and Autonomous Systems*, vol. 112, 2019.
64. T. Salam and M. A. Hsieh, “Adaptive sampling and reduced-order modeling of dynamic processes by robot teams,” *IEEE Robotics and Automation Letters*, vol. 4:no. 2, 2019.
65. T. M. Morse, S. R. Lockery, and T. C. Ferrée, “Robust spatial navigation in a robot inspired by chemotaxis in *caenorhabditis elegans*,” *Adaptive Behavior*, vol. 6:no. 3-4, 1998.
66. P. N. Edwards, *Representing the global atmosphere: Computer models, data, and knowledge about climate change*. MIT Press Cambridge, MA, 2001, vol. 1, ch. Changing the atmosphere: Expert knowledge and environmental governance.
67. M. Vergassola, E. Villermaux, and B. I. Shraiman, “‘infotaxis’ as a strategy for searching without gradients,” *Nature*, vol. 445:no. 7126, 2007.
68. L. Peng, D. Lipinski, and K. Mohseni, “Dynamic data driven application system for plume estimation using uavs,” *Journal of Intelligent & Robotic Systems*, vol. 74:no. 1, 2014.
69. S. Li, Y. Guo, and B. Bingham, “Multi-robot cooperative control for monitoring and tracking dynamic plumes,” in *2014 IEEE International Conference on Robotics and Automation (ICRA)*, IEEE, 2014.
70. J. Wainwright and M. Mulligan, *Environmental modelling*. Wiley Online Library, 2002.
71. A. Kucukelbir, D. Tran, R. Ranganath, A. Gelman, and D. M. Blei, “Automatic differentiation variational inference,” *J. Mach. Learn. Res.*, vol. 18:no. 1, 2017.
72. P. Chevaldonné, D. Desbruyères, and M. Le Haître, “Time-series of temperature from three deep-sea hydrothermal vent sites,” *Deep Sea Research Part A. Oceanographic Research Papers*, vol. 38:no. 11, 1991.
73. C. E. Rasmussen and C. K. Williams, *Gaussian processes for machine learning*. MIT Press MIT Press, 2004, vol. 14.

74. N. Metropolis, A. W. Rosenbluth, M. N. Rosenbluth, A. H. Teller, and E. Teller, “Equation of state calculations by fast computing machines,” *The journal of chemical physics*, vol. 21:no. 6, 1953.
75. A. R. Conn, N. I. Gould, and P. L. Toint, *Trust region methods*. SIAM, 2000.
76. L. M. Miloshevich, A. Paukkunen, H. Vömel, and S. J. Oltmans, “Development and validation of a time-lag correction for vaisala radiosonde humidity measurements,” *Journal of Atmospheric and Oceanic Technology*, vol. 21:no. 9, 2004.